Heat transfer and transport property contrast effects on the compressible Rayleigh-Taylor instability

Kevin Cherng and Sanjiva Lele

Department of Mechanical Engineering, Stanford University, Stanford, California 94305, USA

Daniel Livescu ⓘ

*CCS-2 Computational Physics and Methods, Los Alamos National Laboratory,
Los Alamos, New Mexico 87545, USA*

In extreme environments, the Rayleigh-Taylor instability (RTI) may occur under large variations in density and temperature and with fluid transport properties strongly dependent on temperature. Direct numerical simulations of the 3D fully compressible RTI are conducted, examining the idealized configuration of a hotter, less dense fluid pushing against a colder, denser fluid. Various temperature ratios and transport property configurations are explored to examine how heat conduction, large variations in transport properties, and sudden changes in transport properties can affect the evolution of the mixing layer. Nonuniform fluid expansion and contraction induced by heat transfer can significantly affect local density differences and overall instability growth, causing profile asymmetries about the initial interface for flow and mixing statistics. The departures from classical self-similar development of the instability along with misalignment between regions of mixing and regions of most intense turbulent activity caused by both heat transfer and transport property contrasts are examined. After sudden changes in fluid transport properties, which may occur as a result of rapid heating (e.g., in inertial confinement fusion), the flow quickly responds and begins to relax towards quasi-self-similar late-time evolution. For many dynamical quantities such as vorticity and dissipation, this late-time evolution resembles that of the configuration that already started with the final transport property magnitudes, suggesting that these quantities depend only on the transport properties and not on past flow history, provided that the density field distributions for the flows remain similar. On the other hand, the mixing evolution after the transport property change is unique, implying that both property magnitudes and previous history are impactful on the mixing. These simulations demonstrate how various temperature-related effects are extremely important to consider in compressible RTI flows with large temperature variations.

DOI: 10.1103/PhysRevFluids.9.043904

I. INTRODUCTION

The Rayleigh-Taylor instability (RTI) most generally occurs when fluids are accelerated opposite to their density gradient [1–4]. Small perturbations at the interface grow, developing spikes of heavier fluid and bubbles of lighter fluid, which interact nonlinearly and eventually transition the flow to turbulence. RTI development is influenced the strongest by the local density ratios, but parameters such as compressibility, initial perturbation spectrum, temperature distribution, viscosity, surface tension, mass diffusion, geometry, and magnetic fields can also have important effects. In certain extreme situations, the RTI may occur under large variations in density and fluid transport properties of viscosity, thermal conductivity, and mass diffusivity, through either temperature variations or differences in the fluid properties themselves. In inertial confinement fusion (ICF), the dense walls,

also known as ablator material, of an imploding fuel capsule are decelerated by the less dense but more viscous compressed gas at the center, with temperature differences up to 10^7 K [5]. In a supernova event, the exploding dense ejecta from the core is decelerated by the less dense, hotter surrounding circumstellar matter, reaching temperature variations of 10^9 K [6]. Earth's mantle-core interactions and oceanic flows may also involve large variations in fluid density/buoyancy and viscosity.

This paper focuses on exploring the effects of heat transfer due to a nonuniform background temperature and temperature-dependent transport properties on the 3D compressible RTI. Currently, most fully compressible simulations of the RT instability have started with a uniform initial background temperature and assumed the fluids have equivalent, constant transport properties [7–13]. It has been theorized that thermal conduction during the coasting/deceleration stage of an ICF implosion and the formation of supernova remnants may significantly change the structure of the interface and lead to very different instability progression [6,14]. Should the heat flux be strong enough, the volumetric expansion of colder fluid regions may be high enough to ablate material away from the interface. A few studies have considered compressible RTI configurations with nonuniform background temperatures but have shown minimal heat transfer effects. The significant differences between configurations with isothermal, isentropic, or isopycnic background stratifications were briefly explored by Wieland *et al.* [15]. Chen *et al.* [16] used the Discrete Boltzmann Method to determine how viscosity and heat conduction can affect the 2D single-mode RT instability.

In ICF applications, there has been significant interest in the ablative RTI (ARTI) [17,18]. In the process called mass ablation during the acceleration phase of an ICF implosion, heat is deposited onto the colder, denser fluid, causing it to expand and ablate off of the outer surface of the interface. This ablated light fluid then pushes back against the heavy fluid in an RT unstable manner. Simulations exploring ARTI typically begin with a fully developed ablative interface, with a nonzero initial velocity field, continuous heating through a boundary heat flux or a heat source in one fluid, and a time-varying gravitational force to fix the interface position. It has been found that the mass ablation has a stabilizing effect in the initial linear regime but a destabilizing effect in the late nonlinear and turbulent regimes. The conditions considered in this paper are not as extreme, the observed heat transfer not strong enough to cause the mass ablation phenomenon.

According to Gerashchenko and Livescu [5], fluid compressibility can be independently characterized apart from the speed of sound/flow compressibility effects by the ratio of specific heats of the fluids participating in the mixing. Compressibility effects may be stabilizing or destabilizing, depending on the configuration [5,19]. The speed of sound, which is set by the equilibrium pressure at the interface, determines the equilibrium density profile. Much work has been done exploring the effects of compressibility in the context of background density stratification [20–22]. The ratio of specific heats determines a fluid's ability to expand or contract in response to heat transfer and pressure fluctuations. However, for the monoatomic ions that occur in high-energy density (HED) plasmas in, for example, ICF, the ratio of specific heats is close to 5/3, while the equation of state is close to ideal. In this case, the atomic/molecular weight ratio, besides directly determining the driving density ratio, also influences the density response to changes in temperature and pressure, as well as the heat capacities through variations in the ideal gas constant, altering the mixing behavior of fluids that have different compositions. The simulations in this work hold the background stratification constant to focus solely on the effects of compressibility in terms of a fluid's ability to change volume due to heat conduction.

In many flows with large variations in transport properties, the fluids involved are HED plasmas with highly temperature-sensitive transport properties. Plasma RT simulations in our specific regime of interest, using particle-in-cell (PIC) or magnetohydrodynamic (MHD) flow solvers, have mostly been limited to either a 2D domain or single-mode perturbations [23,24]. Studies using hydrodynamic solvers specifically focusing on the effects of variable plasma transport properties on mixing have been performed for the 2D RT and Kelvin-Helmholtz instabilities [25] and a spherical mixing layer under adiabatic compression [26]. For non-HED flows, Jaberi, Livescu,

and Madnia [27] compared chemically reacting compressible homogeneous turbulence to canonical incompressible homogenous turbulence, identifying slight differences in turbulence structure that were attributed to temperature-dependent transport property variations. This paper will compare the differences in RT turbulence behavior between fluids with constant transport properties and those with temperature-dependent plasma-type properties.

Further studies have also explored how flows respond to sudden changes in transport properties after mixing and turbulence has sufficiently developed. This occurs in ICF implosions, where the central region called the "hot spot" experiences a significant increase in temperature and therefore viscosity. Livescu and Daniel [28] have explored this using single-fluid forced isotropic turbulence with transport property variations dependent on an evolving scalar field that can represent either temperature or concentration. According to G. I. Taylor's hypothesis, at high enough Reynolds numbers, dissipation is independent of viscosity [29]. This has been confirmed in variable density turbulent mixtures, where velocity gradients quickly adapt to changed spatially varying viscosity fields, eventually leading to uniform dissipation throughout the domain, as if the viscosity change had never been applied [30]. Similar results have been found in subsequent work for variable-conductivity mixtures and scalar dissipation [31]. We examine if RT turbulence with significant heat transfer and transport property contrasts still exhibits dissipation-viscosity independence.

In this paper, we present a comprehensive analysis of how heat conduction, large variations in transport properties, and sudden changes in transport properties affect the development of the 3D fully compressible Rayleigh-Taylor instability. Starting from isothermal baseline cases, we vary both the temperature ratio and transport property behavior. We explore how the initial instability growth, structure of the mixing interface, transition to turbulence, and fluid mixing is affected in the presence of large temperature gradients and temperature-dependent fluid transport properties. In our simulations, we begin to approach conditions where one fluid has low enough viscosity to easily transition to turbulence, while the other fluid has high enough viscosity that fully developed turbulence cannot be sustained. Section II defines the governing equations and the nondimensional parameters for the compressible RTI, the problem setup with description of the different transport property configurations, and the numerical methods used for the DNS calculations. Section III presents all the results, including the typical basic RTI flow characterizations, detailed analysis of the flow dynamics and mixing state, and particular focus on the flow's response to transport property changes. Section IV puts the results of our idealized variable-temperature setup in context of real-world situations and describes some of the numerical difficulties associated with large transport property contrasts. The primary conclusions and discussion of future work are in Sec. V.

II. PROBLEM DESCRIPTION

A. Governing equations

We solve the fully compressible Navier-Stokes equations for two miscible ideal gas species, with the bottom fluid labeled (1) and the top fluid labeled (2). The variables are nondimensionalized as follows: density ρ by the initial density difference $\rho_0 = [\rho(z_{\text{int}}^+) + \rho(z_{\text{int}}^-)]/2$, position $\vec{x}$ by the length scale L_0, velocity $\vec{u}$ by the velocity scale based on free fall velocity over a distance L_0 (same as gravity wave speed) $\sqrt{gL_0} = U_0$, pressure P by $\rho_0 U_0^2$, time t by $\sqrt{L_0/g}$, energy $E = \rho(e + \vec{u} \cdot \vec{u}/2)$ by $\rho_0 U_0^2$, and temperature T by $U_0^2/C_{p,0}$, where $C_{p,0}$ is the specific heat at constant pressure of the top fluid and e is the mixture's internal energy. The quantity z_{int} is the initial interface position shown in Fig. 1 and L_0 is related to the most unstable wavelength. The nondimensionalization of transport properties and the nondimensional parameters (Re, Pr, Sc) use the upper fluid (2) properties at a reference pressure and temperature. With mass fraction Y_i, viscosity $\mu^* = \mu/\mu_0$, bulk viscosity $\beta^* = \beta/\beta_0$, thermal conductivity $\kappa^* = \kappa/\kappa_0$, mass diffusivity $D^* = D/D_0$, ideal gas constant $R^* = R/R_0$, ratio of specific heats γ, and enthalpy $h_i^* = h_i/\rho_0 U_0^2$, the governing
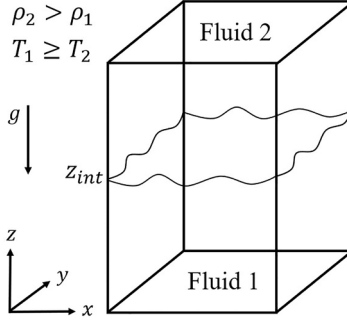
FIG. 1. Schematic of the RT instability problem.

equations in nondimensional form are the following:

$$\frac{\partial(\rho^*Y_i)}{\partial t^*} + \vec{\nabla}^* \cdot (\rho^*\vec{u}^*Y_i) = -\frac{1}{\text{ReSc}}\vec{\nabla}^* \cdot \vec{J}_i^*, \tag{1}$$

$$\frac{\partial(\rho^*\vec{u}^*)}{\partial t^*} + \vec{\nabla}^* \cdot (\rho^*\vec{u}^* \otimes \vec{u}^*) = -\vec{\nabla}^*P^* + \frac{1}{\text{Re}}\vec{\nabla}^* \cdot \boldsymbol{\tau}^* + \rho^*\vec{g}^*, \tag{2}$$

$$\frac{\partial E^*}{\partial t^*} + \vec{\nabla}^* \cdot [(E^* + P^*)\vec{u}^*] = -\vec{\nabla}^* \cdot \left(\frac{1}{\text{Re}}\boldsymbol{\tau}^* \cdot \vec{u}^* - \frac{1}{\text{RePr}}\vec{q}_c^* - \frac{1}{\text{ReSc}}\vec{J}_d^*\right) + \rho^*\vec{g}^* \cdot \vec{u}^*, \tag{3}$$

$$P^* = (1 - 1/\gamma)\rho^*\bar{R}^*T^* \quad \text{with} \quad \frac{1}{\bar{M}} = \frac{Y_1}{M_1} + \frac{Y_2}{M_2}, \quad \bar{R} = \frac{R_u}{\bar{M}}, \quad \gamma = 5/3, \tag{4}$$

where the Reynolds, Prandtl, and Schmidt numbers are

$$\text{Re} = \frac{\rho_0 U_0 L_0}{\mu_0}, \quad \text{Pr} = \frac{C_{p,0}\mu_0}{\kappa_0}, \quad \text{Sc} = \frac{\mu_0}{\rho_0 D_0}. \tag{5}$$

The gravitational force points downwards such that $\vec{g}^* = -\delta_{i3}$. We use Fickian mass diffusion fluxes,

$$\vec{J}_i^* = -\rho^*D_i^*\vec{\nabla}Y_i, \tag{6}$$

Newtonian viscous stress vector,

$$\boldsymbol{\tau}^* = \mu^*(\vec{\nabla}^*\vec{u}^* + \vec{\nabla}^*\vec{u}^{*T}) + \left(\beta^* - \tfrac{2}{3}\mu^*\right)(\vec{\nabla}^* \cdot \vec{u}^*)\boldsymbol{\delta}, \tag{7}$$

conductive heat flux

$$\vec{q}_c^* = -\kappa^*\vec{\nabla}^*T^*, \tag{8}$$

and the interspecies diffusion heat flux

$$\vec{J}_d^* = \sum_i h_i^*\vec{J}_i^*. \tag{9}$$

From this point forward, the asterisks signifying the nondimensionalization are dropped from all variables and expressions for clarity, unless indicated otherwise.

B. Software and numerical methods

The PadeOps software developed at the Stanford Flow Physics and Aeroacoustics Laboratory uses a tenth-order compact finite difference scheme for calculation of spatial derivatives and a fourth-order Runge-Kutta time-stepping scheme for time discretization. Details of the numerical algorithms can be found in Ref. [32]. The software originally solves the governing equations in

conservative form, where the fluxes in Eqs. (1)–(3) are calculated before the divergence operator is applied, so any second derivatives are evaluated using two applications of the first derivative operator. To increase solution accuracy and stability, we solve the equations in nonconservative form, which contain terms expanded with the chain rule so the resulting derivatives of transport properties and the second derivatives are directly calculated. For example, the viscous terms are expanded as

$$\frac{\partial}{\partial x_j}(\tau_{ij}) = \frac{\partial \bar{\mu}}{\partial x_j}\left(\frac{\partial u_i}{\partial x_j} + \frac{\partial u_j}{\partial x_i}\right) + \bar{\mu}\left(\frac{\partial^2 u_i}{\partial x_j^2} + \frac{\partial^2 u_j}{\partial x_i \partial x_j}\right) + \frac{\partial}{\partial x_j}\left(\bar{\beta} - \frac{2}{3}\bar{\mu}\right)\frac{\partial u_k}{\partial x_k}\delta_{ij}$$

$$+ \left(\bar{\beta} - \frac{2}{3}\bar{\mu}\right)\frac{\partial^2 u_k}{\partial x_j \partial x_k}\delta_{ij}. \tag{10}$$

The species mass diffusion and thermal conduction terms are treated similarly. This ensures that the effect of viscosity and other transport properties is properly applied at the Nyquist wavenumber, critical for maintaining stability when no subgrid models, filtering, or localized artificial diffusion (LAD) is used in the main body of the solution. Additionally, the convective terms in the governing equations are expanded into a skew-symmetric form that has been shown to reduce aliasing errors [33]:

$$\frac{\partial(\rho Y_i u_j)}{\partial x_j} = \frac{1}{2}Y_i\frac{\partial(\rho u_j)}{\partial x_j} + \frac{1}{2}\rho u_j\frac{\partial Y_i}{\partial x_j} + \frac{1}{2}\frac{\partial(\rho Y_i u_j)}{\partial x_j}, \tag{11}$$

$$\frac{\partial(\rho u_i u_j)}{\partial x_j} = \frac{1}{2}u_i\frac{\partial(\rho u_j)}{\partial x_j} + \frac{1}{2}\rho u_j\frac{\partial u_i}{\partial x_j} + \frac{1}{2}\frac{\partial(\rho u_i u_j)}{\partial x_j}, \tag{12}$$

$$\frac{\partial((\rho e_t + P)u_j)}{\partial x_j} = \frac{1}{2}e_t\frac{\partial(\rho u_j)}{\partial x_j} + \frac{1}{2}\rho u_j\frac{\partial e_t}{\partial x_j} + \frac{1}{2}\frac{\partial(\rho e_t u_j)}{\partial x_j} + \frac{\partial(Pu_j)}{\partial x_j}. \tag{13}$$

The code has been verified with successful replication of results from 2D single-mode RT simulations conducted by Gauthier and Crueuer [7]. Additionally, further tests confirmed that in general symmetry is maintained and that the numerics support a stable interface when no perturbations are present.

C. Initial conditions

We consider the classical Rayleigh-Taylor instability configuration of a denser fluid (2) above a less dense fluid (1) under a constant gravitational acceleration. The domain is $4L_0 \times 4L_0 \times 10L_0$ at a resolution of $512 \times 512 \times 1280$. Beginning with an isothermal ambient atmosphere base case of two moderately stratified exponential density fluid layers under hydrostatic equilibrium, we then investigate cases where the fluids begin at different but uniform temperatures and have different transport property configurations. In our variable temperature simulations, we choose the lower, light fluid to be hotter, in order to mimic ICF hot spot conditions. The equations for the 1D background profiles of density $\rho(z)$, mass fraction $Y_i(z)$, and pressure $P(z)$ used in our simulations have been developed by Creurer and Gauthier [7]; example profiles are shown in Fig. 2. The density $\rho(z)$ and other profiles are constructed from regularized Heaviside functions $H\pm(z) = [1 \pm \text{erf}(z/\delta)]/2$ with an initial interface length scale δ:

$$\rho(z) = (1 + \text{At})\exp(A_- z)H_+(z) + (1 - \text{At})\exp(A_+ z)H_-(z), \tag{14}$$

$$Y_1(z) = (1 + \text{At})\exp(A_- z)H_+(z)/\rho(z)Y_2(z) = 1 - Y_1(z), \tag{15}$$

$$p(z) = p_b + (1-\text{At}^2)\left\{e^{A_- z}H_+(z) + e^{A_+ z}H_-(z) - \frac{1}{2}\left[e^{\Lambda_-^2}\text{erf}\left(\frac{z}{\delta} - \Lambda_-\right) - \frac{1}{2}e^{\Lambda_+^2}\text{erf}\left(\frac{z}{\delta} - \Lambda_+\right)\right]\right\}\bigg/\text{Sr}, \tag{16}$$
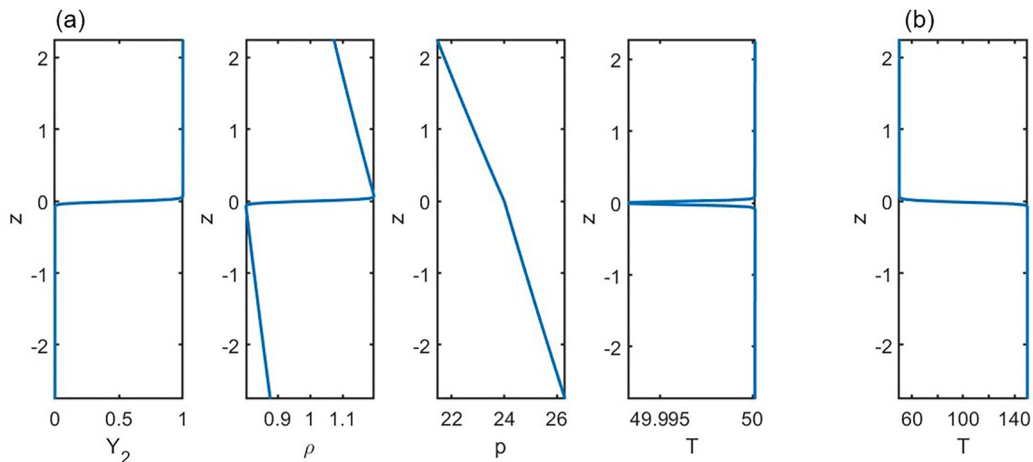
FIG. 2. (a) Nondimensional mass fraction, density, pressure, and temperature profiles for the isothermal base case and (b) nondimensional temperature profile for the temperature ratio three cases.

where $A_\pm = -\text{Sr}/(1 \pm \text{At})$, $\Lambda_\pm = A_\pm \delta/2$ and p_b is the integration constant that satisfies the isothermal temperature boundary conditions, as pressure is determined analytically by integrating the density. Note that away from the interface, the temperature becomes constant, but different on the two sides of the interface, except for the isothermal case. The ideal gas assumption is used to calculate $T(z)$:

$$T(z) = \frac{P(z)}{\rho(z)\bar{R}(z)}, \quad \frac{1}{\bar{M}(z)} = \frac{Y_1(z)}{M_1} + \frac{Y_2(z)}{M_2}, \quad \bar{R}(z) = \frac{R_u}{\bar{M}(z)}, \tag{17}$$

where M_i are the molecular masses of each species. The Atwood number defined in terms of the density at both sides of the interface or the molecular mass ratio and temperature ratio is

$$\text{At} = \frac{\rho_2(z_{\text{int}}^+) - \rho_1(z_{\text{int}}^-)}{\rho_2(z_{\text{int}}^+) + \rho_1(z_{\text{int}}^-)} = \left(\frac{M_2}{M_1}\frac{T_1}{T_2} - 1\right) \bigg/ \left(\frac{M_2}{M_1}\frac{T_1}{T_2} + 1\right) \tag{18}$$

or equivalently

$$\frac{M_2}{M_1} = \frac{1 + \text{At}}{1 - \text{At}}\frac{1}{T_1/T_2}. \tag{19}$$

This setup for the background state enables easy exploration of various Atwood numbers, temperature ratios, and stratification strengths.

While Eq. (18) shows that there is only one unique mass fraction ratio M_1/M_2 for each At for an isothermal background state, we can increase the bottom fluid (hot spot) temperature in the variable temperature cases by adjusting the molecular masses M_1 and M_2, effectively changing the average gas constant $\bar{R}$, so that the initial concentration, density, and pressure profiles remain the same as in the base cases. For an At of 0.2, an isothermal case will have a molecular mass ratio $M_1/M_2 = 2/3$, while a case with a temperature ratio $T_1/T_2 = 3$ will have $M_1/M_2 = 2$. Maintaining the density profile is important for keeping the interface Atwood number constant between cases, so any difference in the instability development can be directly attributed to the changes in temperature. Furthermore, it is not possible to vary the temperature and preserve the initial density and hydrostatic pressure profiles without changing the composition of the initial interface, which would complicate mixing comparisons. Due to these restrictions, there is only one unique molecular mass ratio M_1/M_2 per each parameter set of temperature ratio and Atwood number.

TABLE I. Simulation parameters for the isothermal base case; δ is the initial interface length scale described in Ref. [7].

Re	Sc	Pr	At	Sr	$\gamma_1 = \gamma_2$	δ
10 000	1	1	0.2	0.04	5/3	0.031

D. Transport property configurations

Three different transport property configurations are explored in the variable temperature simulations, with the intent to systematically separate the effects of nonuniform background temperature and temperature-dependent transport properties. The first *constant property* configuration assumes that both fluids have equal and constant transport properties. When compared to the isothermal case, the effects of heat transfer are isolated. The second *variable property* configuration assumes the fluid transport properties obey a plasma-type temperature scaling. According to kinetic theory, shear viscosity, diffusion constant, and thermal conductivity for HED plasmas in ICF applications can approximately obey the power law $\mu \propto T^{2.5}$, $D \propto T^{2.5}$, and $\kappa \propto T^{2.5}$ [34]. Bulk viscosity is zero because plasmas can be modeled as monoatomic ions. For the variable transport property cases, a nondimensionalized transport property (represented by ϕ) variation is

$$\phi(T) = \left(\frac{T}{T_0}\right)^{2.5}, \tag{20}$$

where T_0 is the temperature of the upper fluid that does not change temperature between cases. For a temperature ratio of 3, the transport property magnitude contrast is approximately 15.6. The third *transitional property* configuration begins with constant transport properties, but after some time has elapsed, the coefficients are artificially modified to reflect their dependence on the temperature field. This approximates one of the fluids quickly heating up after the instability has progressed for some time, such as during the formation of the hot spot in ICF. For these transitional cases, the transport properties are implemented as

$$\phi(t, T) = (1 - \xi_\phi) + \left(\frac{T}{T_0}\right)^{2.5} \xi_\phi, \tag{21}$$

$$\xi_\phi(t) = 0.5 + 1/2\mathrm{erf}((t - t_t)/\tau_t) \tag{22}$$

with transition time $t_t = 8.5$, a transition timescale of $\tau_t = 0.1$, and initial upper fluid temperature T_0. The transition time t_t occurs after the flow has reached a sufficiently turbulent state. Signs that the flow has transitioned to turbulence can be observed in the plots of penetration depths (Fig. 8) and dissipation [Fig. 22(a)], but the most important criterion we use is that the velocity spectrum has developed a classical turbulent inertial range. We apply the transport property change in our transitional property cases as soon as possible due to the limited domain size. The function $\xi_\phi(t)$ has an initial value of 0 and a final value of 1, with τ_t chosen so there is a fast but smooth transition (as opposed to a step function or a gradual change) at the time the temperature dependence is turned on. The proper, physically realistic method to simulate fluid heating is to add a heat source term to the energy equation. However, this is likely to introduce strong pressure waves, which will interfere with flow development [35]. Artificially manipulating the transport properties as described will allow us to avoid such complications and completely isolate the transport property effects.

E. Nondimensional parameters

The nondimensional parameters provided in Table I that characterize the simulations use transport property magnitudes (μ, κ, D) referenced to the upper fluid, which remains at a constant temperature across simulations. In the variable transport property configurations, the actual Re is much lower in the hotter fluid, significantly increasing the influence of heat transfer and mass
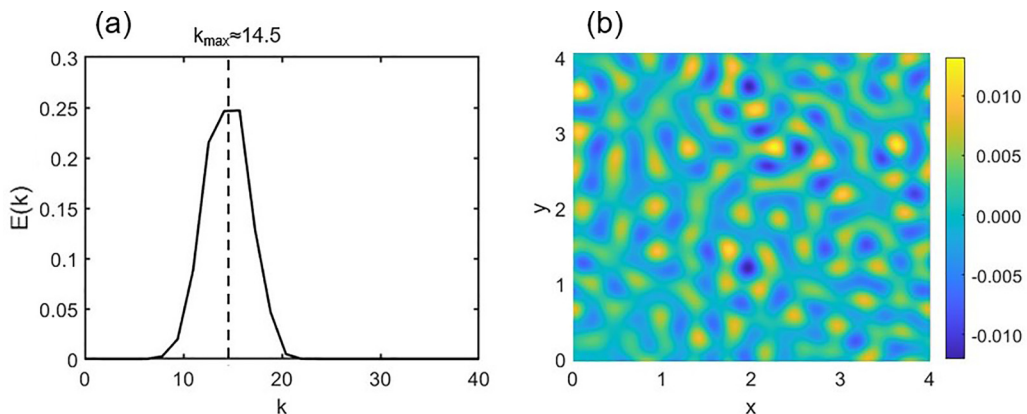
FIG. 3. (a) Normalized spectrum $E_\eta(k)$ of the initial perturbations in wavenumber space, dashed line indicates the most unstable wavenumber for the 2D version of the problem; (b) the initial perturbations in physical space.

diffusion there. The Reynolds number is based on free-fall velocity over a distance L_0, $U_0 = \sqrt{gL_0}$, and length scale L_0 that is near the maximum wavelength of the applied initial perturbations. The domain is moderately stratified with a stratification parameter $\text{Sr} = gL/(T_r R/M_r)$ of 0.04. Other literature on compressible RT choose to parametrize stratification using the isothermal Mach number $M = \sqrt{\rho g L/P}$ at the interface, which is related to Sr with $M^2 = \text{Sr}$ using the ideal gas equation. The Schmidt number and Prandtl number are both set to 1 for generality. Typically, a Sc of $O(1)$ and low Pr to represent high thermal conductivity are used for a very crude approximation of plasma properties [36]. Specific heat ratios of $\gamma = 5/3$ is a good approximation for monoatomic plasma ions.

F. Initial perturbations

Defining the wavenumbers as $k_x = 2\pi/\lambda_x$ and $k_y = 2\pi/\lambda_y$, where λ_x, λ_y are the perturbation wavelengths in the two horizontal directions, we apply a randomized multimode perturbation $\eta(x, y, z)$ to the 1D background profiles Eqs. (14)–(17), turning them into perturbed fields in all three dimensions:

$$\eta(x, y, z) = \text{real}\left[\sum_i \sum_j a_{ij} \exp(ik_{x,i}x) \exp(ik_{y,j}y) \exp(-2\pi|z - z_{\text{int}}|) \right], \tag{23}$$

$$\rho_{\text{pert}}(x, y, z) = \rho(z + \eta(x, y, z)), \quad Y_{\text{pert}}(x, y, z) = Y(z + \eta(x, y, z)),$$

$$T_{\text{pert}}(x, y, z) = T(z + \eta(x, y, z)), \quad p_{\text{pert}}(x, y, z) = p(z + \eta(x, y, z)), \tag{24}$$

where a_{ij} is the magnitude corresponding to the set of wavenumbers $(k_{x,i}, k_{y,j})$. The a_{ij} and their corresponding wavenumber values are stored for reproducibility of the results. Note that $k_{x,i}$ and $k_{y,j}$ can be chosen to be negative. These perturbations to the background profiles decrease in intensity away from the initial interface location $z_{\text{int}} = 5.5$. The spectrum $E_\eta(k)$ of $\eta(x, y, z_{\text{int}} = 5.5)$ is Gaussian in $k = \sqrt{k_x^2 + k_y^2}$ wavenumber space with the peak located at $k_{\text{max}} \approx 14.5$, a standard deviation of $\frac{2}{3}\pi$, and has a total perturbation energy per area of $\int_0^{L_x} \int_0^{L_y} \eta(x, y, z_{\text{int}}) \, dx \, dy/L_x L_y = 1.2E - 5$. The value of k_{max} corresponds to most unstable mode of the equivalent 2D version of this problem. Note that L_0 is approximately the wavelength corresponding to the left tail of the spectrum distribution, where the value of $E_\eta(k)$ approaches 0 in Fig. 3. All simulations begin with the same initial perturbations.
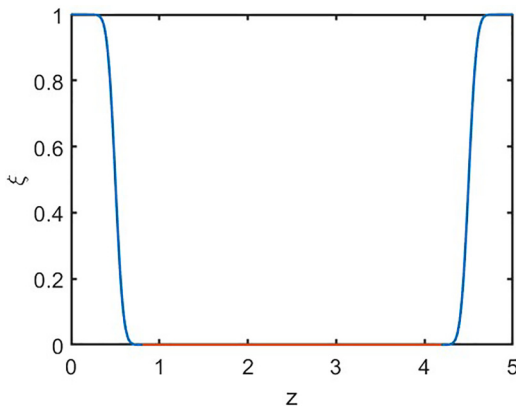
FIG. 4. Example mask function ξ used for boundary filtering; red region indicates where the mask is exactly zero.

G. Boundary conditions

Most simulations of the RTI apply slip walls at the top and bottom of the domain, but in compressible simulations this allows acoustic waves to reflect off the boundary and potentially influence instability growth and turbulent behavior. Instead, we leave the boundaries open to approximate an infinite domain. While a tenth-order compact finite difference scheme is used to calculate derivatives in the main body of the solution, we apply a general boundary closure for the last few points at the boundary, with a fourth-order one-sided stencil for the boundary point, a fourth-order stencil for the second point, a sixth-order stencil for the third point, and so on. However, if this boundary treatment is applied by itself, numerical errors will add up over time as the simulation progresses and cause boundary node instability, especially because the stratified background causes many variables to have nonzero derivatives at the boundary. To stabilize the boundary nodes and eliminate the effects of any acoustic waves that reach the boundary, we need to apply a few other boundary treatments. We create a boundary diffusion zone by adding a forcing term and a numerical diffusion term to the governing equations (1)–(3):

$$\frac{\partial \boldsymbol{U}}{\partial t} = \boldsymbol{F}(\boldsymbol{U}) + \nu_d \xi_d \frac{\partial^2 \boldsymbol{U}'}{\partial x_j \partial x_j} - C_f \xi_f \boldsymbol{U}', \tag{25}$$

where $\boldsymbol{U} = (\rho Y_i, \rho u_i, E)$ are the evolved quantities, $\boldsymbol{U}' = \boldsymbol{U} - \boldsymbol{U}_{\text{background}}$ are the perturbations from the initial/background state, and ξ_d and ξ_f are the diffusion and forcing term mask functions, an example of which can be seen in Fig. 4. The forcing term forces the solution at the boundary towards the initial background state, while the diffusion term is required to maintain numerical stability. The numerical diffusion coefficient is defined as

$$\nu_d = C_d \frac{\Delta x^2}{2\Delta t} \tag{26}$$

in which $C_d = 1$ corresponds to the stability limit of a general advection-diffusion equation. We also apply a nonreflecting boundary that removes the energy of reflecting waves using the Navier-Stokes characteristic boundary conditions (NSCBC) methodology [11].

The boundary antialiasing filtering is implemented as

$$\boldsymbol{U} \to (1 - \xi)\boldsymbol{U} + \xi\widetilde{\boldsymbol{U}}, \tag{27}$$

where $\widetilde{\boldsymbol{U}}$ is the filter applied on the conserved quantities $\boldsymbol{U}$ and ξ is the filter mask, which is nonzero only close to the boundaries. This filtering operation on $\boldsymbol{U}$ is applied at every substep

of the time-stepping algorithm. The eighth-order compact filter that is used removes the top 10% of the resolvable wavenumber components. In our simulations, we choose $\xi = \xi_d = \xi_f$.

III. RESULTS

Compared to Boussinesq RT flows, which have well-studied self-similar scalings and symmetries, the behavior of compressible simulations depends on many factors such as stratification strength, compressibility effects, the initial temperature profile, and others. This paper focuses on the differences caused by two fluids starting at different temperatures and different transport property configurations compared to a baseline isothermal case A, briefly characterized in Sec. III A, that already experiences effects from the moderate At and stratification values. Starting with a basic characterization of all the flow cases through various Reynolds numbers, length scales, and examination of self-similar behavior in Sec. III B, we then closely examine how changes in the density field affect the dynamics of the flows in Sec. III C. Next, we examine how heat transfer and transport property contrasts can influence mixing in Sec. III D. Finally, we discuss how the flow responds to rapid changes in transport properties through the lens of Taylor's viscosity-dissipation independence postulate and turbulence structure in Sec. III E.

A. Isothermal base case

This section briefly describes the isothermal base case. The precise definitions of the quantities plotted in Fig. 5 will be covered in later sections, as explained below. Figure 5(a) shows the spike and bubble penetration depths based on the 5% mole fraction limits (see Sec. III B, Fig. 8 for definition). With a moderate Atwood number of 0.2, there is asymmetric development of the spikes and bubbles, with penetration of the spikes into lower-density fluid higher than the penetration of the bubbles into higher-density fluid. A transition from the initial exponential growth of the spikes and bubbles to the beginning of a self-similar mixing stage can be seen at around $t = 8$. Figure 5(b) plots the horizontally averaged mole fraction profiles against the vertical position scaled by the mixing height at various times (see Sec. III B, Fig. 9 for definition). The curves at later times collapse into a self-similar profile. The asymmetry of spike/bubble side growth and spatial self-similarity of quantities such as average density or average concentration has been well documented in variable-density RTI literature [37,38]. The time evolution of the θ mix parameter (see Sec. III D, Fig. 19 and Eq. (39) for definition) is plotted in Fig. 5(c). The general temporal evolution of θ, along with the final value of about 0.8, is also in line with previous literature [21,37,39]. Figure 5(d) contains plots of the Favre turbulent kinetic energy ($\rho u_i'' u_i''/2$) and dissipation rate of turbulent kinetic energy ϵ, volume averaged within the extents of the mixing zone (see Sec. III E, Fig. 22 and Eq. (31) for definition). This volume-averaging operation is represented by $\langle \rangle_\Omega$. Due to the stratified background density, the development of TKE and dissipation will be different from typical Boussinesq results, since the spikes need to push into increasingly heavy fluid while the bubbles rise into increasingly lighter fluid. The growth of TKE does not transition directly into the t^2 incompressible self-similar scaling, instead reaching a peak value followed by a slight trough, behavior that has been observed in previous simulations of compressible RTI [9]. The magnitude of the dissipation rate reaches a peak near the onset of turbulent mixing and then slowly decays. In more highly stratified conditions, the turbulence will display a stronger decaying regime and dissipation decreases much more rapidly [9], up to total suppression of the instability [12].

B. Basic flow characterization

The flow is periodic in the transverse directions, so the planar averages are taken in the direction perpendicular to the direction of gravity. Angle brackets or overbars are used to denote the planar averages, unless otherwise indicated. We decompose the velocity (u, v, w), density ρ, pressure p, and specific volume υ into Reynolds ($u = \langle u \rangle + u'$) and Favre ($u = \langle \rho u \rangle / \langle \rho \rangle + u'' = \tilde{u} + u''$) averages and their associated perturbations. The turbulent kinetic energy $\tilde{k}$, transverse Taylor length
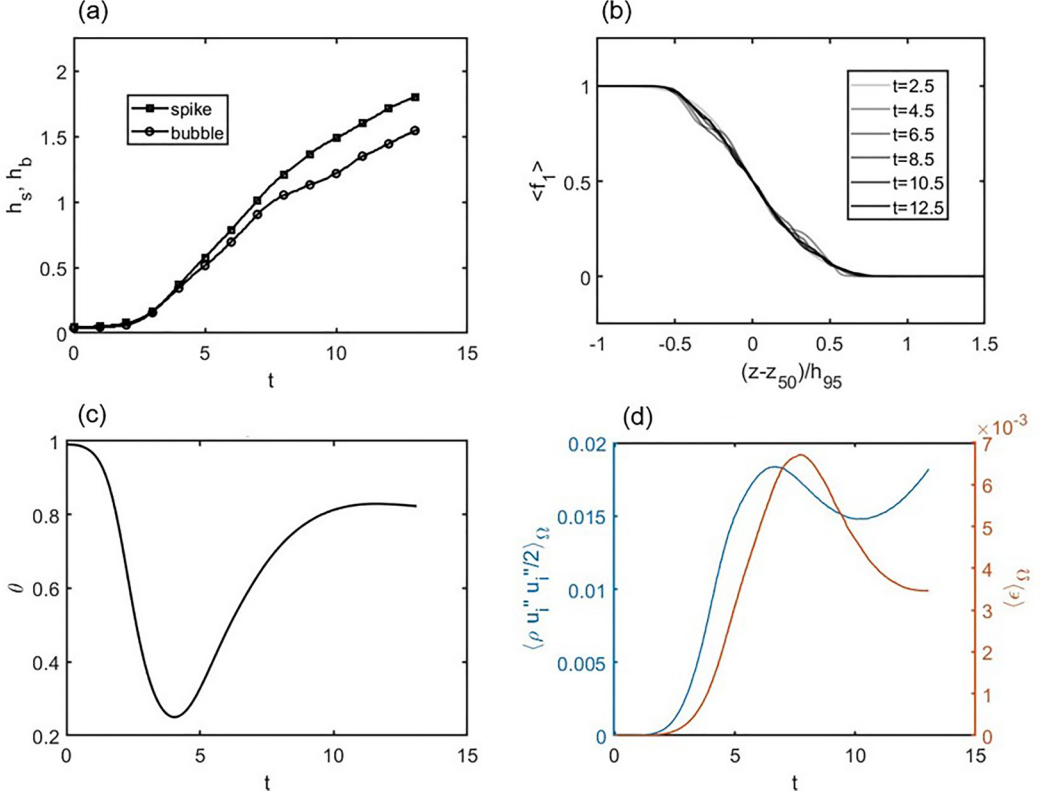
FIG. 5. (a) Time history of the spike and bubble side penetration depths based on the 5% average mole fraction limits (Sec. III B, Fig. 8). (b) Average mole fraction $\langle f_1 \rangle$ profiles at various times, centered around the mixing midplane location z_{50} and scaled by mixing height h_{95} (Sec. III B, Fig. 9) (c) Time history of Young's mixing parameter θ [Sec. III D, Fig. 19, Eq. (39)]. (d) Time history of the average Favre turbulent kinetic energy and the average dissipation rate of turbulent kinetic energy ϵ, volume averaged within the mixing zone [Sec. III E, Fig. 22, Eq. (31)].

scale λ_{xx}, vertical Taylor length scale λ_{zz}, and dissipation rate of turbulent kinetic energy ϵ are defined as

$$\tilde{k} = \langle \rho u_i'' u_i'' \rangle / (2\bar{\rho}), \tag{28}$$

$$\lambda_{xx}^2 = \frac{\overline{u''^2}}{\left(\frac{\partial u''}{\partial x}\right)^2}, \tag{29}$$

$$\lambda_{zz}^2 = \frac{\overline{w''^2}}{\left(\frac{\partial w''}{\partial z}\right)^2}, \tag{30}$$

$$\epsilon = \left\langle \tau_{ij}' \frac{\partial u_i'}{\partial x_j} \right\rangle, \tag{31}$$

where $\tau_{ij}' = \mu s_{ij}'$ and $s_{ij}' = \frac{\partial u_i'}{\partial x_j} + \frac{\partial u_j'}{\partial x_i} - \frac{2}{3} \frac{\partial u_k'}{\partial x_k} \delta_{ij}$.
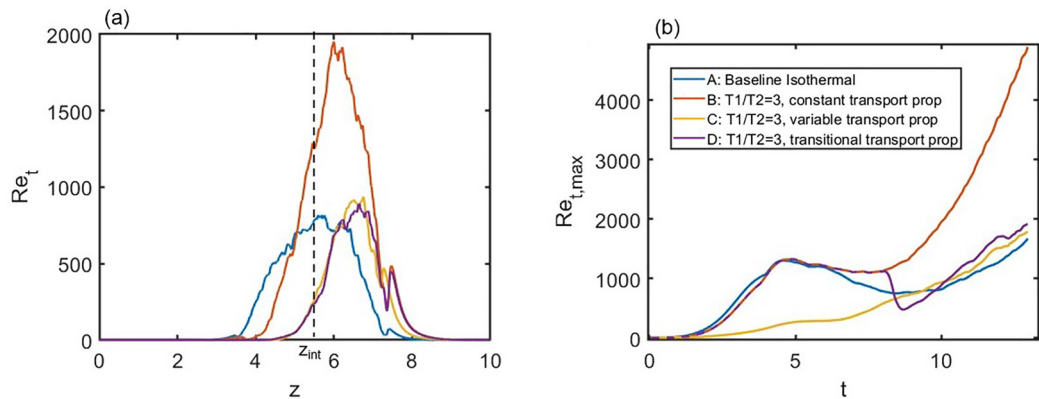
FIG. 6. (a) Vertical variation of the turbulent Reynolds number at $t = 10$ for all cases, with the dashed line indicating the location of the initial interface position z_{int}; (b) time history of the maximum turbulent Reynolds number for all cases.

The turbulent Reynolds number and Taylor Reynolds numbers, all a function of vertical position z, are defined as

$$\mathrm{Re}_t = \frac{\tilde{k}^2 \bar{\rho}}{\bar{\nu}\epsilon},$$ (32)

$$\mathrm{Re}_{\lambda xx} = \frac{\sqrt{2\tilde{k}}\lambda_{xx}}{\bar{\nu}},$$ (33)

$$\mathrm{Re}_{\lambda zz} = \frac{w_{\mathrm{rms}}\lambda_{zz}}{\bar{\nu}},$$ (34)

where w_{rms} is the root-mean-square value of the vertical velocity at each z plane and $\bar{\nu}$ is the average kinematic viscosity. The Kolmogorov length scale η is

$$\eta = \left(\frac{\bar{\nu}^3 \bar{\rho}}{\epsilon}\right)^{1/4}.$$ (35)

The extra $\bar{\rho}$ in Eqs. (32) and (35) is required for consistency with our definition of ϵ.

The turbulent Reynolds number in RT mixing is best interpreted as the ratio between turbulent eddy viscosity and molecular diffusivity and can also be considered as a measure of the scale separation in the energy spectrum. It is importantly proportional to the quantity $\tilde{k}^2/\epsilon$, which is used for estimating the eddy viscosity in many gradient transport turbulence models. As seen in Fig. 6, it rises from zero at the edges of the flow and peaks somewhere within the mixing zone, but not at the initial interface position $z_{int} = 5.5$ for most cases. Heat transfer in case B slightly shifts the peak of turbulence upwards and adding the transport property dependencies in case C shifts the peak further into the heavy fluid region. Due to the large transport property contrasts in cases C and D, the vertical variation of all the Reynolds numbers becomes highly asymmetric about z_{int}. After the transition to turbulence at around $t = 8$, both the Taylor and turbulent Reynolds numbers increase over time until the simulation ends at $t = 13$. For the transitional property case D, the transport property change is applied at $t = 8.5$, and the time of $t = 10$ represents a time at which the flow has had ample time to respond to the property changes. The Re_t values of the constant property case B greatly exceed those of all our other cases after the transition to turbulence; the detailed explanation for this phenomenon is covered in Sec. III C.

The Taylor Reynolds numbers $\mathrm{Re}_{\lambda xx}$ and $\mathrm{Re}_{\lambda zz}$ are based on the horizontal λ_{xx} and vertical λ_{zz} Taylor microscales and their associated velocity scales. The Taylor microscales characterize the length scales at which viscosity begins to influence the flow eddies and approximately marks the

TABLE II. Description of all four cases and various metrics of the flow taken at the final simulation time.

Label	T_1/T_2	Transport property	$\mathrm{Re}_{t,\max}$	$\mathrm{Re}_{\lambda xx,\max}$	$\mathrm{Re}_{\lambda zz,\max}$	$k_{\max}\eta_{\min}$
A	1	Constant (isothermal)	1700	150	220	1.4
B	3	Constant	4900	220	390	1.4
C	3	Variable	1800	150	250	2.1
D	3	Transitional	1900	150	240	2.1

threshold between the inertial subrange and dissipative scales. As expected for highly anisotropic flows, the vertical Taylor Reynolds number is approximately 1.6 times as large as the horizontal one at all times. The spatial and temporal evolution of $\mathrm{Re}_{\lambda xx}$ and $\mathrm{Re}_{\lambda zz}$ are similar to that of Re_t displayed in Fig. 6. Table II contains the maximum Taylor and turbulent Reynolds numbers inside the mixing region at the final simulation time. In previous fully resolved simulations of variable-density RT turbulence, $\mathrm{Re}_t \approx 4600$ had been achieved at At = 0.5 [38] and $\mathrm{Re}_t \approx 6000$ at At = 0.75 [40], corresponding to a Taylor Reynolds number Re_λ based on the istropic turbulence formula (i.e., $\mathrm{Re}_\lambda = \sqrt{20/3\mathrm{Re}_t}$) of approximately 175 and 200, respectively. At these Reynolds numbers, some scale separation between the production and dissipative scales is expected. In fully compressible RTI simulations, Gauthier [9] reached a maximum $\mathrm{Re}_{\lambda zz}$ of 76 while Luo and Wang [21] reached a $\mathrm{Re}_{\lambda zz}$ of 65.7, although both explored highly stratified density configurations where $\mathrm{Re}_{\lambda zz}$ does not monotonically increase the entire simulation. The values reached in the current work are significantly higher.

The dimensionless parameter $k_{\max}\eta_{\min}$ based on the maximum resolvable wavenumber is $k_{\max} = 2\pi/(2\Delta x)$ using grid size Δx characterizes the resolution of the simulation. A $k_{\max}\eta_{\min}$ of 1.4–1.5 is adequate for resolving average values of quantities such as ϵ, but not for quantities involving higher-order moments of velocity gradients [41,42]. Higher $k_{\max}\eta_{\min}$ is required for capturing extreme velocity events, which are rare at the moderate Reynolds numbers explored here, especially in cases C and D with higher viscosity in the lower fluid. Therefore, we expect all our direct numerical simulations to have fully resolved statistics. The scale resolution is further characterized below where the energy spectra are discussed. Cases C and D, with the higher viscosity and mass diffusivity values, are better resolved for all the dissipative scales. In this problem, full resolution of the dissipative scales of molar concentration is especially important because we closely examine regions where significant molecular mixing occurs.

We choose a mixing height definition based on the 5% average mole fraction $\langle f \rangle$ limits. The spike/bubble side penetration depths h_s, h_b are defined as the vertical distance between the initial interface position z_{int} and the z location where the average mole fraction is 0.05/0.95, and the mixing height is $h_{95} = h_s + h_b$. In non-Boussinesq compressible RT flows, the mole fraction profiles display less asymmetry than when using mass fraction or density [40]. Assuming self-similarity, the mixing height grows (in dimensional terms) according to

$$h = \alpha \mathrm{At}gt^2 + 2(\alpha \mathrm{At}gh_0)^{1/2}t + h_0, \tag{36}$$

and the growth rate α can be estimated with

$$\alpha = \left(\frac{h(t)^{1/2} - h(t_0)^{1/2}}{(\mathrm{At}g)^{1/2}(t - t_0)} \right)^2, \tag{37}$$

where t_0 in general can be an arbitrary time during self-similar growth stage [43,44]. This similarity method has been shown to be more robust than estimating α with the time derivative of h and is capable of providing a good estimate before the mixing layer width reaches the asymptotic t^2 growth. While derived for Boussinesq RT flows, the model has been shown to apply to variable-density cases with Atwood numbers up to 0.9 [40]. Equation (37) can be plotted against simulation time t for various t_0 values. If the chosen t_0's are during the mixing layer's self-similar growth period,
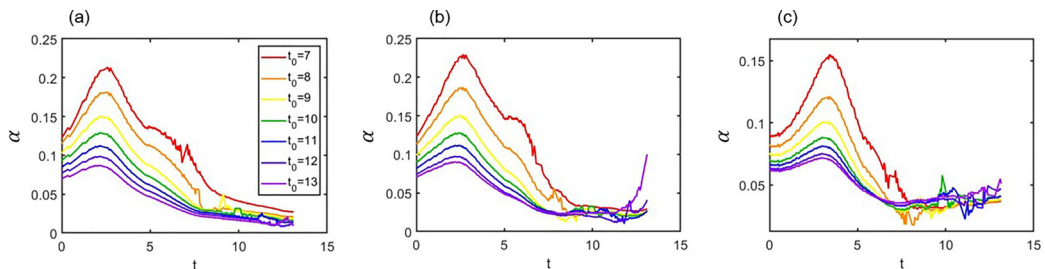
FIG. 7. Estimates of the growth rate α calculated for various t_0 values using Eq. (37) for (a) isothermal case A, (b) T1/T2 = 3 constant property case B, and (c) T1/T2 = 3 variable property case C.

then all the curves should theoretically converge on a flat value of α when $t > t_0$. The earliest time t_0 that can successfully estimate a stable value of α marks the point when the turbulent mixing layer growth is becoming self-similar [43]. The curves in Fig. 7 suggest that all the flows reach an approximately self-similar state past $t \approx 8$. To estimate α, values are sampled from the relatively flat portions of the $t_0 = 8, 9, \ldots, 13$ curves and then averaged. Table III contains the average and standard deviations of the sampled α values for cases A to C, along with comparisons to other relevant simulations that begin with short-wavelength initial perturbations and experiments. The value of α obtained is about 0.023 for the isothermal and constant property cases and about 0.036 for the variable property case. Note that none of the flows have developed to a point where the t^2 term in Eq. (36) is dominant. These α values are in line with other similar compressible simulations but lower than typical experimental values [37,38,45].

Figure 8 indicates that the mixing height as a whole does not differ much between the isothermal, constant property and transitional property cases, but the behaviors of the spike and bubble sides differ significantly. At the moderate At of 0.2 used here, there is slight asymmetry in the mixing layer penetration depths, with the spikes falling faster than the bubbles ascending. Compared to the baseline isothermal case A, both the heat transfer alone in the constant property case B and the transport property contrast in the variable property case C slow spike side penetration after about $t = 7$. For the temperature ratio of 3 explored here, the large-scale effects of heat transfer are not apparent until the onset of self-similar mixing layer growth at approximately $t = 8$, which happens to coincide with the change in slope of penetration depths (Fig. 8) and in the saturation of dissipation [Fig. 22(a)]. For the variable property case, the initial spike side penetration is higher because of the increased mass diffusion in the hotter, bottom fluid. The effects of heat transfer and transport properties on bubble penetration are more complicated. Due to background density stratification and the non-Boussinesq density ratio, the bubble growth rate in the isothermal case A slows slightly after

TABLE III. Comparisons of the growth rate α with results from other simulations and experiments in the literature.

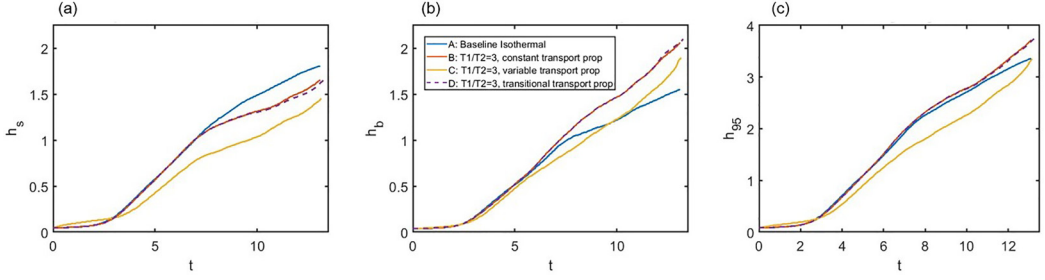| Case	α
A: Baseline isothermal (DNS)	0.023 ± 0.006
B: T1/T2 = 3 constant property (DNS)	0.023 ± 0.005
C: T1/T2 = 3 variable property (DNS)	0.036 ± 0.005
Cabot and Cook [38,44,46] (DNS)	0.02
Livescu $et\ al.$ [44] case RT2 (DNS)	0.02
Youngs [47] case A (LES)	0.027
Dimonte $et\ al.$ [45] (aggregated simulation results)	0.025 ± 0.003
Dimonte $et\ al.$ [45] (aggregated experimental results)	0.057 ± 0.008

FIG. 8. Time history of (a) spike penetration depths, (b) bubble penetration depths, and (c) mixing heights based on the 5% mole fraction limits.

$t = 8$. We can observe that the bubble side penetration in cases B and C displays no such slowing and eventually exceeds that of the isothermal case A. Detailed examination and explanation of this phenomenon are in the next section. In general, the sudden transport property changes in case D are not strong enough to affect the average large-scale motions within the layer.

Figure 9 displays the average mole fraction profiles as a function of vertical position at various times after the mixing layer has reached the self-similar regime for cases A, B, and C. The z coordinate is shifted so that $z = 0$ corresponds to the location of the mixing midplane, defined as the point where the average mole fraction $\langle f_1 \rangle$ is 0.5, and is also scaled with the mixing width h_{95}. The mixing midplane location z_{50} is not a fixed point, instead moving into the light fluid side as time advances, due to asymmetries in the spike and bubble sides penetrations. Note that the time histories of z_{50} and the corresponding $\langle f_1 \rangle = 0.05, 0.95$ locations z_5 and z_{95} can be found in Fig. 15. Normalizing the z position in this manner collapses the mole fraction profiles for our baseline case A very well, and is moderately successful in collapsing the profiles for cases B and C. Heat transfer appears to preferentially suppress turbulent diffusion on the light fluid side, causing the mole fraction profile to gradually sharpen over time, while the heavy fluid side profile remains self-similar.

Figure 10 displays the average density profiles using the same z-coordinate normalization with z_{50} and h_{95}. For case A, the density profiles exhibit some deviation from self-similarity on the heavy fluid side. Cases B and C display much weaker self-similarity, especially in the heavy fluid regions, suggesting that heat transfer causes misalignment between mixing (which affects mole fraction) and turbulent behavior (which is strongly influenced by density).

C. Interface structure and flow dynamics

The major differences in spike/bubble side penetration and turbulent behavior described before can be attributed to the conductive heat transfer and its effects on the density field. There is heat
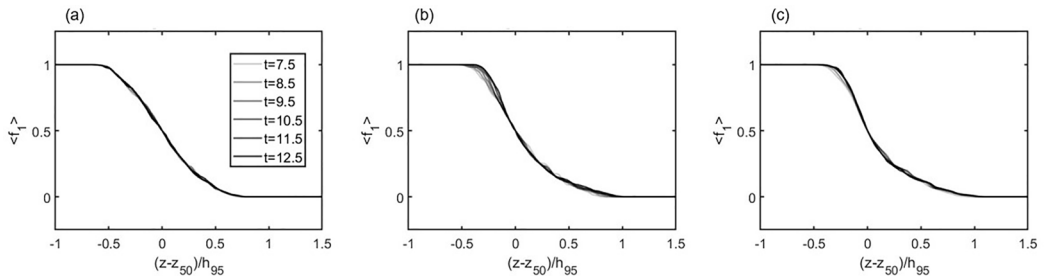

FIG. 9. Average mole fraction $\langle f_1 \rangle$ profiles at various times, centered around the mixing midplane location and scaled by mixing height h_{95} for (a) isothermal case A, (b) $T1/T2 = 3$ constant property case B, and (c) $T1/T2 = 3$ variable property case C.
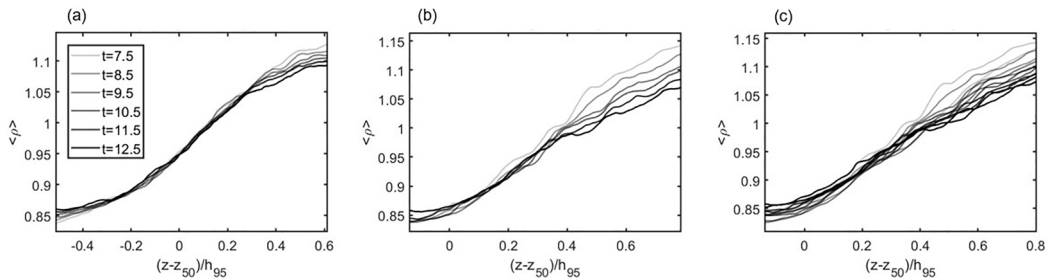
FIG. 10. Average density $\langle \rho \rangle$ profiles at various times, centered around the mixing midplane location and scaled by mixing height h_{95} for (a) isothermal case A, (b) T1/T2 = 3 constant property case B, and (c) T1/T2 = 3 variable property case C.

flux from the hotter lower fluid to the colder upper fluid, causing expansion of the heavy fluid and contraction of the light fluid. The heat flux is local to the interface, as there is no volumetric heat source or heat flux entering from the boundaries. Considering the ideal gas equation $P = \rho RT$, provided that pressure remains relatively constant near the interface, when the temperature changes, the density inversely changes proportional to the magnitude of the ideal gas constants, or equivalently the molecular masses of the gas. Therefore, the intensity of expansion or contraction depends on the temperature ratio of the two gases and magnitude of ideal gas constants. Due to the setup requirements of the temperature ratio cases, the ideal gas constant of the upper fluid is twice as large as that of the lower fluid ($R_2 > R_1$). The falling spikes of heavy fluid will expand more vigorously than how much the rising bubbles contract. These differences affect the local density values, which can be quantified by a local Atwood number, and greatly influence the strength and direction of buoyancy forces acting on the flow.

Figures 11 and 12 display a vertical slice of density during the nonlinear growth stage and the turbulent stage of the instability, respectively. At early times, neither the heat transfer nor the increased viscosity in cases B and C causes major changes in the structure of the spike and bubble sides. A closer inspection reveals that the spikes in case B are slightly thinner than those in case A, and that the spikes in case C lack both the characteristic mushroom-head shape and any clear vortical structures that are typically generated at the spike tips. At late times, there are obvious
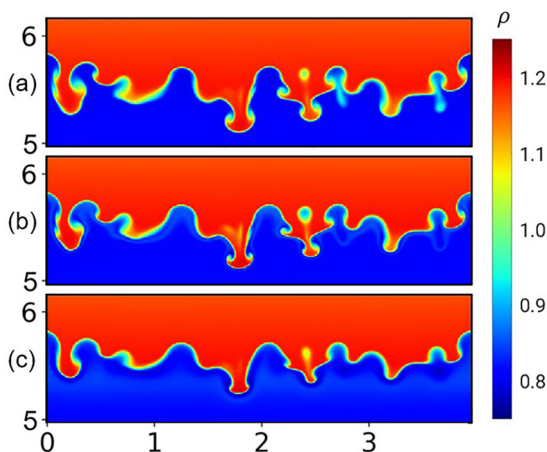

FIG. 11. Comparison of early time ($t = 4$) density contours at the interface for (a) isothermal case A, (b) T1/T2 = 3 constant property case B, and (c) T1/T2 = 3 variable property case C.
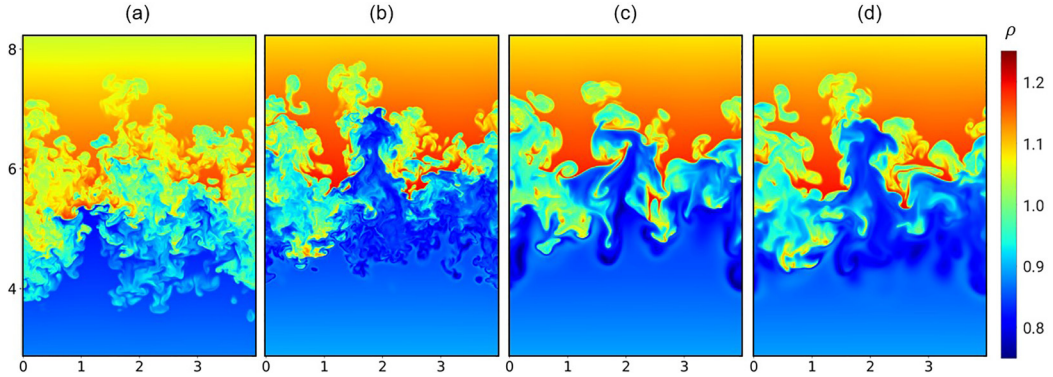
FIG. 12. Comparison of late time ($t = 12$) density contours at the interface for (a) isothermal case A, (b) T1/T2 = 3 constant property case B, (c) T1/T2 = 3 variable property case C, and (d) T1/T2 = 3 transitional property case D.

differences. With the heat transfer in the variable temperature cases, the distribution of local density difference magnitudes is altered, including density reversals in the hotter fluid side, where the falling spikes become less dense than the surrounding background fluid. Additionally, heat transfer causes larger density differences to be maintained for a longer period of time in the cold fluid side. It is important to note that this is an effect dependent on the molecular masses of the two fluids, and that simulations exploring different or opposite molecular mass ratios could have drastically different results. Applying transport property contrasts in C and D increases the average bubble/spike size and decreases the range of scales in the turbulent flow.

Figure 13 follows the evolution of a single, representative spike in the variable property case C. The series of figures shows the cold spike gradually equilibrating in temperature with the surrounding, hotter background fluid. The spike undergoes notable volumetric expansion, represented by the dark red positive dilatation and the surrounding fluid slightly contracts, represented by the barely visible light blue, negative dilatation, a consequence of the upper fluid being more compressible than the lower fluid. The density contours show the spike gradually becoming less dense than the surrounding light fluid, causing buoyancy forces to act in the opposite direction and reversing instability progress on the light fluid side of the interface. Conductive heat transfer is the dominant source of fluid dilatation in these simulations. Although pressure waves are generated at the simulation initiation and throughout the entire duration of the instability due to spikes and bubbles acting as pistons [48], they are not strong enough to significantly affect any of the flow dynamics.

Figure 14 follows the evolution of a single bubble in the variable property case C. We observe the same progress towards temperature equilibrium as observed with the spikes. However, with heat conduction, the light fluid in the bubble barely contracts and the surrounding heavy fluid undergoes expansion, enveloping the bubble with less dense, formerly heavier fluid. Again, this is indicated by the darker red, positive dilatation of the upper fluid and the lighter blue, negative dilatation in the plots of velocity divergence. This causes the bubble penetration to be initially delayed and maintains density differences longer to extend the instability progress on the heavy fluid side. As shown in Fig. 12, the local density differences decrease over time in the upper region as the two fluids mix, but the average magnitude of density differences remains larger in cases B, C, and D compared to case A. Since case C has much higher thermal conductivity in the bottom fluid than case B, the effects of heat transfer are felt much sooner in case C. However, once temperature equilibrium is reached between the spikes/bubbles and the surrounding fluid at late times, the final density distributions for cases B and C are remarkably similar.
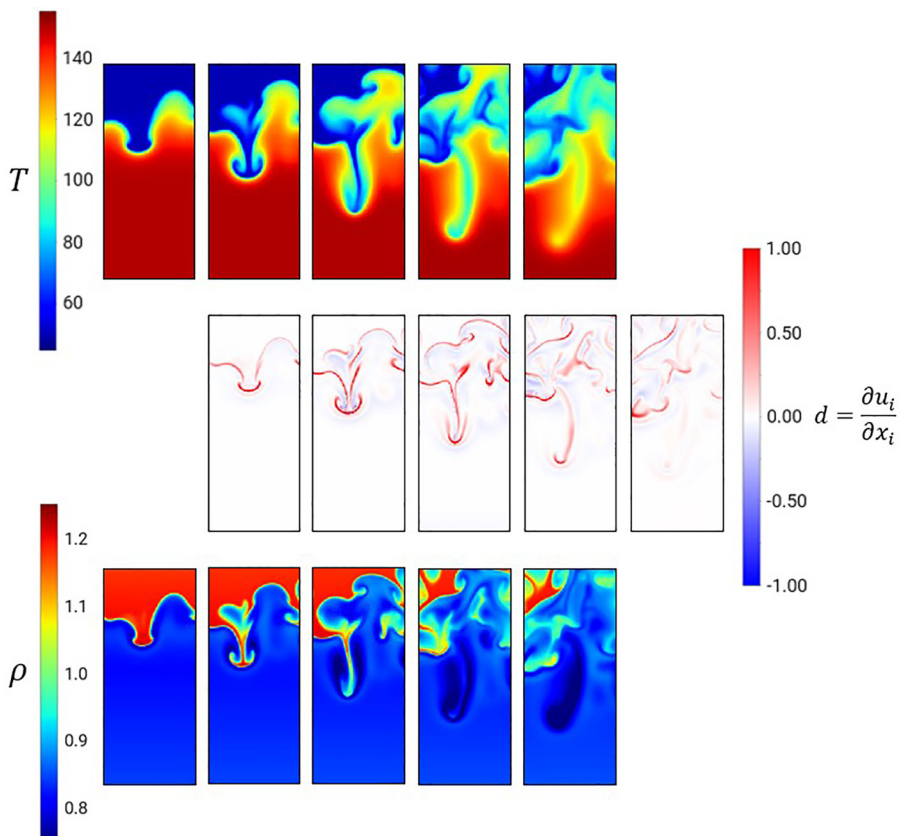
FIG. 13. Visualizations of temperature, dilatation and density tracking the evolution of a single spike in the variable property case C for $t = 4, 5, 6, 7, 8$.

Figure 15 highlights the misalignment between mixing and turbulent activity caused by heat transfer and variation in transport properties. The upper and lower solid lines indicate the mixing extent determined by the 0.05 and 0.95 average mole fraction $\langle f \rangle$ locations, and the central solid line indicates the location of the mixing midplane at $\langle f \rangle = 0.5$. The location of the mixing midplane does not stay at the initial interface position but drifts downwards into the light fluid for all cases. The dashed lines indicate the extent of the most turbulent region, defined as the locations where turbulent Reynolds number Re_t is at least 80% of the peak Re_t in the domain at that given point in time. This is the region where velocity fluctuations ($t < 8$) and turbulent activity ($t > 8$) are strongest, and mixing is dominated more by stirring compared to mass diffusion. In the isothermal case A, the velocity fluctuations start relatively symmetric about the mixing midplane, but then the most intense turbulent activity prefers the heavier fluid side. Heat transfer itself in case B shifts turbulent activity upwards, while the transport property contrast in case C shifts it even further into the heavier fluid. The flow responds to the transport property change in D by immediately shifting the turbulent region extents to approximately the position in case C, where the flow had started with the variable transport properties from the beginning. Compared to case A, the region of highest turbulence is narrower in cases B, C, and D.

Figure 16 shows the weighted vorticity PDF at the plane of highest average vorticity magnitude in the flow after case D has had time to respond to the transport property change at $t = 10$. The area under the curve gives the vorticity variance. The vorticity distribution is not sensitive to heat transfer, as the curves for case A and B are similar, but highly dependent on the magnitude of viscosity,
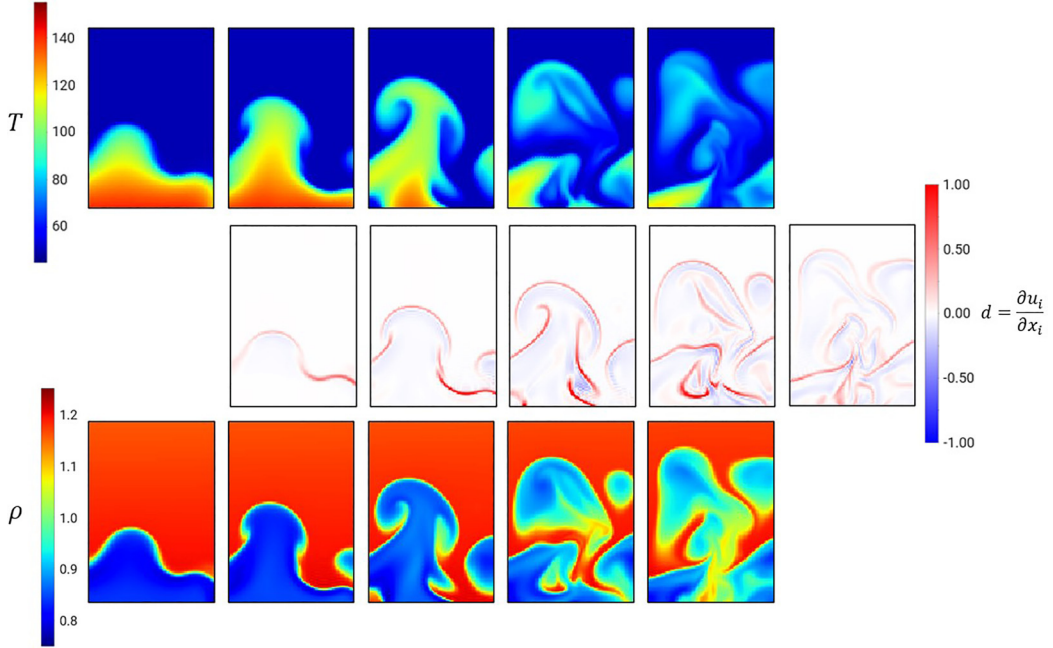
FIG. 14. Visualizations of temperature, dilatation and density tracking the evolution of a single bubble in the variable property case C for $t = 4, 5, 6, 7, 8$.

comparing cases A and C. As expected, higher viscosity decreases both the average magnitude and range of the vorticity values in the flow. Interestingly, vorticity appears to depend only on the current viscosity field, since both the flows that start with C and transition to D end up with similar viscosity fields and vorticity distributions.

The spatial intermittency F_A is defined as the fraction of the flow that can be considered turbulent or above a certain vorticity threshold. The threshold chosen is the magnitude corresponding to 1% of the vorticity variance magnitude at the plane of highest vorticity. The plots of intermittency, with height z normalized by the mixing midplane location and mixing height, are shown in Fig. 16. The peak intermittency of the isothermal case A is slightly misaligned with the center of mixing at $z/h_{95} = 0$, but the turbulent fraction profile is mostly symmetric around the peak value. Note that even at the center of the mixing region, there are still some small regions of laminar flow for all cases. Agreeing with earlier results, the heat transfer in cases B, C, and D causes severe misalignment between the turbulent regions and the plane $z/h_{95} = 0$. These cases also experience a more steep drop in turbulent area fraction in the light fluid side compared to the heavy fluid side.

Due to buoyancy forces, the intensity of turbulent vertical velocity fluctuations is directly proportional to the magnitude of local density differences, which can be quantified by a local Atwood number that compares the magnitude of local density perturbations with the average density. However, typical definitions of the local Atwood number [49] are unable to account for density reversals, which can occur in isothermal, compressible RT flows where the density of the surrounding fluid near the tips of the spikes or bubbles becomes more or less dense than the fluid density inside the spikes/bubbles. In our cases with heat transfer, the density inversions, particularly in the light fluid side, are much more extreme and play a huge part in the flow dynamics. We introduce a metric, PDFs of a signed local Atwood number $At_l = \rho'/\langle \rho \rangle$, that can properly capture the effects of any density reversals. Note that attempting any averaging operation on At_l would destroy much of the relevant information, since its interpretation changes depending on the location within the mixing zone. On the light fluid side, positive At_l values are regions with the falling spikes
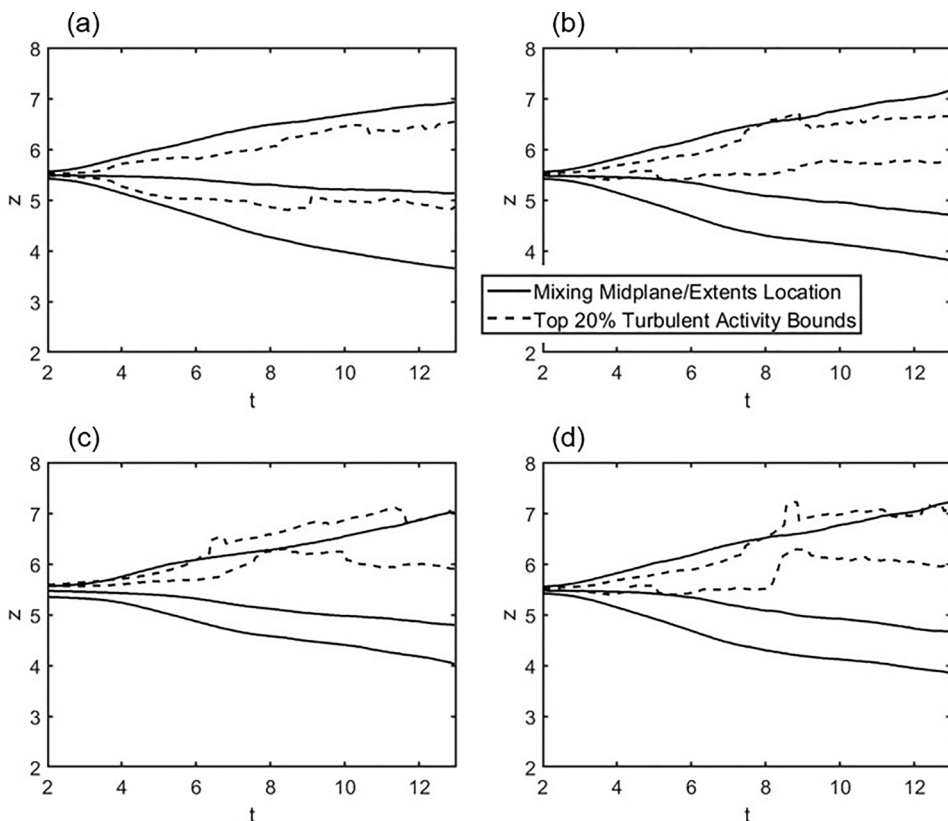
FIG. 15. Time history comparison of the 0.95, 0.5, and 0.05 average mole fraction $\langle f \rangle$ locations (solid lines) and the boundaries of regions with the highest Re_t (dashed lines) for (a) isothermal case A, (b) T1/T2 = 3 constant property case B, (c) T1/T2 = 3 variable property case C, and (d) T1/T2 = 3 transitional property case D.
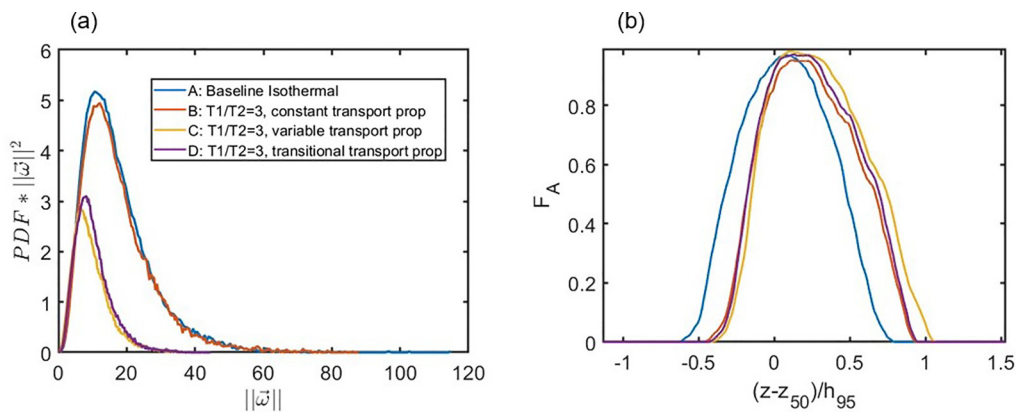

FIG. 16. (a) Weighted vorticity PDF at the plane location of highest average vorticity and (b) the fraction F_A of the plane that is considered turbulent across the mixing layer at time $t = 10$.
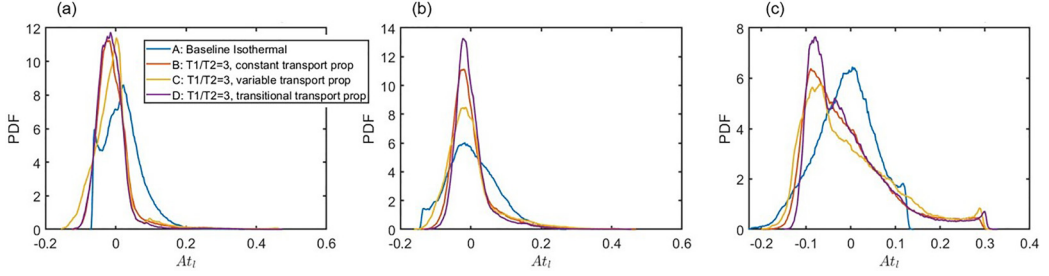
FIG. 17. PDFs of the signed Atwood number inside the turbulent regions at the (a) $\langle f_1 \rangle = 0.75$, (b) $\langle f_1 \rangle = 0.5$, and (c) $\langle f_1 \rangle = 0.25$ plane locations for time $t = 10$.

and negative At_l are the regions with spike regions experiencing density reversal compared to the surrounding light fluid. Conversely, on the heavy fluid side, positive At_l values represent the regions of density inversion and negative At_l values correspond to the rising bubbles. Larger positive At_l values indicate fluid being pulled downwards by gravity, while very negative At_l values indicate fluid regions experiencing strong upward buoyancy forces.

In Fig. 17 we sample only from the turbulent regions to generate the PDFs, in order to prevent the background heavy or light fluids that are not involved in the turbulent mixing from skewing the distributions. On the light fluid side at $\langle f \rangle = 0.75$, there is a higher proportion of negative At_l regions in the variable temperature cases B, C, and D compared to the isothermal case A. The resulting upwards buoyancy forces on the falling spikes experiencing density reversal is responsible for noticeably slowing down the instability progress. With larger temperature ratios and higher heat fluxes, At_l could become negative enough that the spike penetration reverses. At the mixing midplane $\langle f \rangle = 0.5$, both bubbles and spikes are present, along with density reversal effects. With heat transfer, there are fewer extreme negative At_l values and much higher positive At_l values, suggesting a decrease in the intensity of upwards buoyancy forces but much stronger downward gravity forces acting on the flow. In the heavy fluid side at $\langle f \rangle = 0.25$, the frequency of extreme negative or positive At_l values is much higher in the variable temperature cases B, C, and D compared to the baseline case A, indicating much higher gravitational/buoyancy forces and stronger turbulent velocity fluctuations. The prolonged period of sustained density differences in the heavy fluid enabled by heat transfer explains how cases B and C are able to reach such high Re_t compared to the isothermal case A, in which density differences are more quickly diminished. The At_l distributions on the heavy fluid side are similar after temperature has mostly equalized within the mixing layer for all the variable temperature cases. We have shown that many of the differences in instability progress and turbulent intensity can be fully predicted by tracking the At_l behavior.

D. Mixing

Accurately resolving and characterizing the mixing state is important for predicting the level of fuel-ablator mix in ICF applications, or in general, for predicting reaction rates. To analyze the mixing resolution, we can consider the Batchelor scale λ_b, which describes the smallest length scales for concentration fluctuations before molecular diffusion dominates, similar to the Kolmogorov length scale η for velocity/turbulence. We define λ_b as

$$\lambda_b = \left(\frac{\bar{\nu} \bar{\rho} \bar{D}^2}{\epsilon} \right)^{1/4} = \frac{\eta}{\sqrt{\overline{\text{Sc}}}} \quad \text{with} \quad \overline{\text{Sc}} = \bar{\nu}/\bar{D}. \tag{38}$$

Therefore, with our intended computational Schmidt number of 1 in the simulations and the moderate density variations in space due to the moderate $\text{At} = 0.2$ (density is normalized about 1), the mixing should be as well resolved as the dynamics. Figure 18(a) provides the Batchelor scale
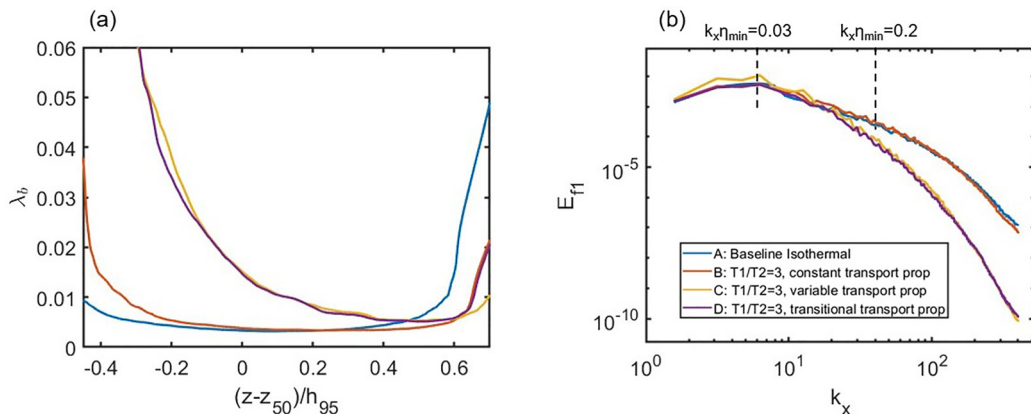
FIG. 18. (a) Spatial variation of the Batchelor scale λ_b at $t = 10$ for all cases, (b) average 1D mole fraction f_1 spectra at the mixing midplane location z_{50} at $t = 10$; the two dashed lines indicate the approximate limits of the inertial range.

λ_b at $t = 10$ for all cases and note that the Kolmogorov scale η has nearly the exact same profiles. Cases A and B have nearly the same minimum mixing length scale, but the heat transfer alone in case B shifts mixing slightly upwards into the heavy fluid, compared to the isothermal case A. The increased molecular diffusivity in cases C and D drastically increases the mixing length scale in the hotter, bottom fluid region.

In Fig. 18(b) the one-dimensional mole fraction fluctuation spectra is examined at the mixing midplane z_{50}. It is calculated using the same method as with the velocity spectra in the next section, taking the Fourier transform in one horizontal direction and averaging along the other horizontal direction. Interestingly, the turbulent fluctuations are very similar for cases A/B and cases C/D. The dashed lines indicate the approximate limits of the inertial range (the expected $-5/3$ scaling) for cases A and B, where $k_x = 2\pi/\lambda_x$ is the 1D wavenumber associated with the wavelength λ_x and η_{min} is the minimum Kolmogorov scale at $t = 10$. Cases C and D at this time have either a very narrow or nonexistent inertial range.

Young's mixing parameter θ, based on the light and heavy fluid mole fractions f_1 and f_2, is used to track the global mixedness:

$$\theta = \frac{\int \langle f_1 f_2 \rangle \, dz}{\int \langle f_1 \rangle \langle f_2 \rangle \, dz}. \tag{39}$$

θ is an integral measure that quantifies the evenness of mixing in each individual horizontal layer in the domain. In the beginning, most layers are composed of either pure light or heavy fluid, so the mixedness metric is high. As the instability grows, the mixedness decreases significantly because the spikes and bubbles create many regions of pure light and heavy fluid in each layer. Eventually, the breakup of the spikes and bubbles and transition to turbulence significantly increases the surface area of the interface, facilitating mixing by molecular diffusion and leading to an increase in the mixedness.

Comparing the isothermal A and variable temperature B cases with constant properties in Fig. 19, we see that heat conduction slightly delays initial instability growth and hinders late-stage mixing, since the rise of θ from the minimum is less steep. Moving from constant to variable transport properties (case B to case C) at the same temperature ratio, we observe a larger delay of instability development and generally a higher level of mixedness due to the boosted molecular diffusion. The immediate boost in mixedness during the property transition in case D can also be attributed to the increase in mass diffusivity.
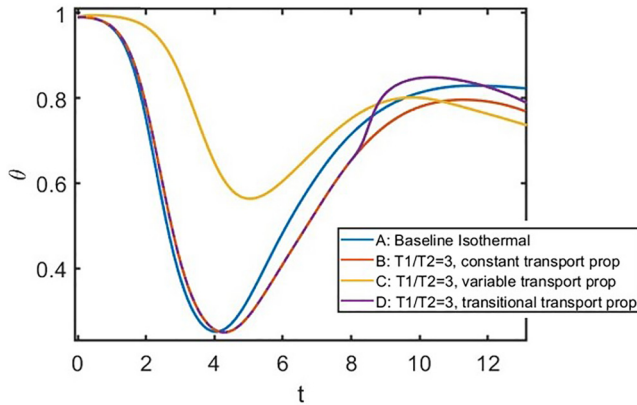
FIG. 19. Time variation of Young's mixing parameter θ.

The density-specific volume correlation $b = -\langle \rho' \nu' \rangle$ is another measure of the mixing state and a very important quantity to understand for turbulence modeling [38]. Typical interpretations are that fully mixed regions have a b value of zero and higher b values suggest a higher potential for future mixing. Figure 20 shows the variation of b both before the transport property adjustment in case D and some time after. In general, the profile of b for the isothermal case A remains approximately symmetric, but heat transfer shifts the peak far into the light fluid side for cases B and C. At the earlier time, the increased mixing by molecular diffusion in case C is reflected in the lower peak value of b. At $t = 10$, the density distributions and corresponding b profiles for the variable temperature cases B, C, and D become quite similar, despite significant differences in mole fraction PDFs in Fig. 21. The isothermal case A has much lower b magnitudes, indicating that the layer has become comparatively much more evenly mixed in terms of density. In incompressible variable density flows where the microscopic densities of the two fluids are constant, b can be a good indicator of mixing, but in compressible flows where other factors can massively influence the density field, b becomes a less useful quantity for assessing mixedness.

Agreeing with previous work on variable density mixing at non-Boussinesq Atwood numbers, the blobs (spikes) of pure heavy fluid are slower to mix compared to the blobs (bubbles) of pure light fluid in the isothermal case [50]. For the baseline case A, the light fluid side at $\langle f \rangle = 0.75$ has
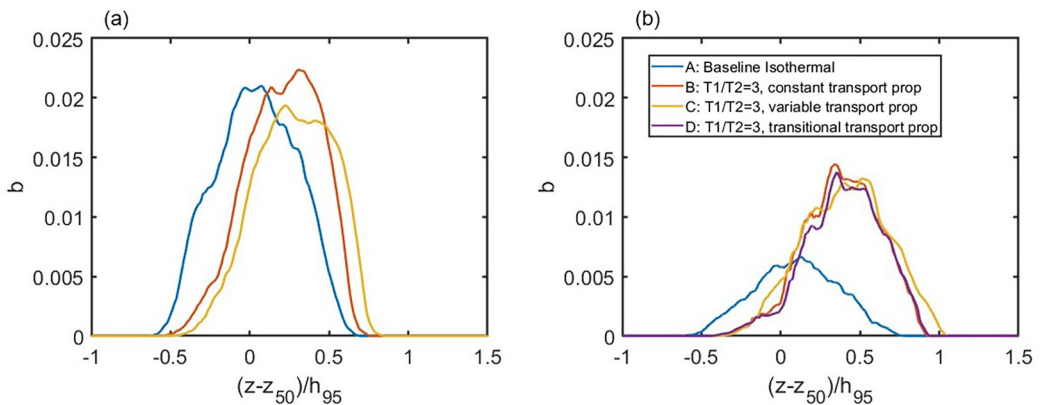
FIG. 20. Spatial variation of the density-specific volume perturbation correlation for (a) $t = 6$ and (b) $t = 10$.
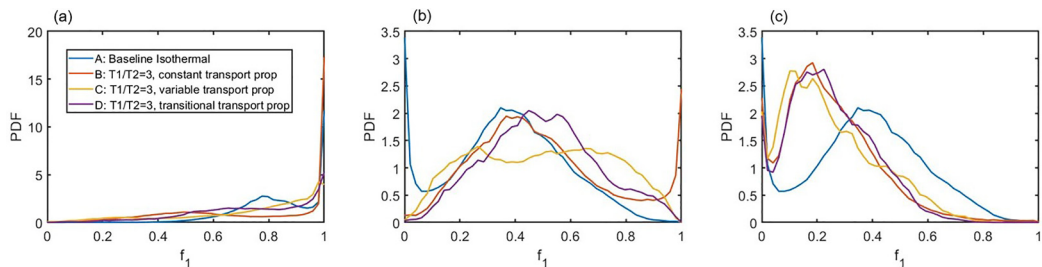
FIG. 21. PDFs of light fluid mole fraction f_1 at the (a) $\langle f_1 \rangle = 0.75$, (b) $\langle f_1 \rangle = 0.5$, and (c) $\langle f_1 \rangle = 0.25$ plane locations for time $t = 10$.

much less heavy fluid from spikes mixed into it, compared to how much light fluid from the bubbles has mixed with the heavy fluid at $\langle f \rangle = 0.25$. The middle of the mixing region for the isothermal case is also highly asymmetric, containing much more pure light fluid than pure heavy fluid. In the lower $\langle f \rangle = 0.75$ plane and at the midplane, heat transfer in case B shifts the peak of distribution towards lower f_1 values, making areas of majority light fluid less common. The increased molecular diffusivity of the light fluid in case C flattens out the mole fraction distributions, increasing the uniformity of mixing for the nonpure fluids. At the upper $\langle f \rangle = 0.25$ plane, both heat transfer and the transport properties cause the mixed fluid to be less uniformly mixed at the molecular level, dragging the bulk of the distributions away from $f = 0.5$.

E. Taylor hypothesis

In this section, we focus on how the flow responds to sudden changes in the transport properties. We examine whether viscosity-dissipation independence applies for fully compressible RT mixtures heavily impacted by heat transfer effects and strong molecular diffusion. We also explore if there is similar behavior for the analogous total mixing rate TMR and mass fraction gradients. The total mixing rate is defined as

$$\text{TMR} = \int D \frac{\partial \rho Y_1}{\partial x_i} \frac{\partial \rho Y_1}{\partial x_i} \, dV. \tag{40}$$

Figure 22(a) shows the time evolution of the volume averaged dissipation magnitude within the extents of the mixing region. For the baseline case A, the dissipation rises until the flow becomes
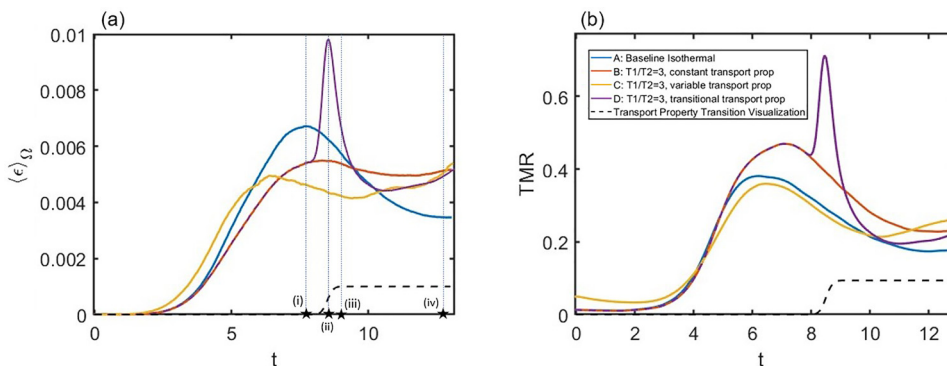

FIG. 22. (a) Time histories of the dissipation of turbulent kinetic energy, domain averaged over the mixing layer extents, and several moments throughout the evolution of case D are highlighted; (b) time histories of the total mixing rate TMR.

fully turbulent, then decays due to the influence of the stratified background. This decay increases with stronger stratification [9]. It appears dissipation is not independent of the heat transfer in case B, as the fluid dilatation and resulting changes to the density field affect the flow dynamics in a major way. The average dissipation is also affected by the transport property contrast applied in case C, likely because the Re in the more viscous light fluid falls far short of the threshold needed for dissipation independence. In the transitional case D, there is a sharp jump in dissipation as the transport property increase is applied, then a relaxation back towards a final state as the velocity gradients adjust. The timescale of the flow relaxation is longer than the timescale of the transport property change. The evolution of case D is highlighted at several moments: (i) corresponds to the moment right before the transport property change is applied, (ii) corresponds to the peak of the response in dissipation, (iii) corresponds to a time during the middle of the flow relaxation, and finally, (iv) corresponds to a time after the flow has reached its long term behavior. Interestingly, the dissipation and its long-time evolution in case D closely resembles the variable transport property case C instead of the original constant transport property case B. This suggests that for these flows with variable properties, as long as the density fields statistics remain similar, the current dissipation levels of the flow depend only on the transport property magnitudes and not on the past flow history.

Similarly, the total mixing rate TMR in Fig. 22(b) is not independent of heat transfer in case B or the transport properties in case C. The heat transfer steepens gradients in ρ and Y while the boosted molecular diffusivity smooths them, causing the higher and lower TMR magnitudes in cases B and C, respectively. In the transitional case D, the general reaction of TMR to the transport property change is similar to that of dissipation, with a peak and relaxation towards a new long-term mixing evolution. However, unlike dissipation, this mixing evolution does not resemble that of cases B or C. This indicates that TMR and more generally the mixing state is dependent not solely on the transport properties, but also on the past history of mixing.

Figure 23 contains average 1D u compensated velocity spectra at the horizontal plane where Re_t is highest (i.e., the peak turbulence location) at various times during the flow response to the change in transport properties of transitional case D. To calculate the spectra, the Fourier transform of u is taken in one direction, then averaged over the other horizontal direction. For all cases, the spectra were found to be independent of the vertical position z inside a portion of the mixing zone, remaining constant at heights ranging from the mixing midplane location to a good distance into the heavy fluid side of the interface, inside of which the most turbulent location is located. Flat regions of the compensated spectra represent the canonical $-5/3$ scaling of the turbulence inertial range. Cases A and B, which have constant properties, have similar spectra indicating fully developed turbulence with a noticeable inertial subrange. Case C with the transport property contrast is still turbulent, but lacks a clear inertial subrange and has a lower turbulent kinetic energy magnitude. During the transition period in case D, the spectra can be observed moving away from the case B spectra towards the case C spectra. As the final state in case D is reached, the spectra for cases C and D are nearly indistinguishable, both in shape and magnitude. Note that the spectra of v, w and turbulent kinetic energy behave similarly. This provides further evidence that after a period of adjustment, many dynamical statistics of the flow conditions explored in this paper depend only on the magnitude of the transport properties. Whether this dependence holds for higher temperature or density ratios is to be explored in further work.

Figures 24(a) and 24(b) display PDFs of the alignment angles between the vorticity vector or mass fraction gradient vector and the eigenvectors of the strain rate tensor. The vorticity-strain angles ξ_1, ξ_2, ξ_3 and mass fraction gradient-strain angles χ_1, χ_2, χ_3 correspond to the eigenvalues $\lambda_1 > \lambda_2 > \lambda_3$ and associated eigenvectors of the strain rate tensor. Again, the statistics are taken from a region surrounding the location of peak turbulence, the most appropriate place to probe the turbulence structure. The alignments for the baseline isothermal case A and the constant property case B qualitatively agree with a wide range of results from incompressible turbulent flows to compressible chemically reacting flows [27]. The vorticity vector prefers to align with the intermediate strain eigenvector, and the mass fraction gradient vector aligns with the most compressive
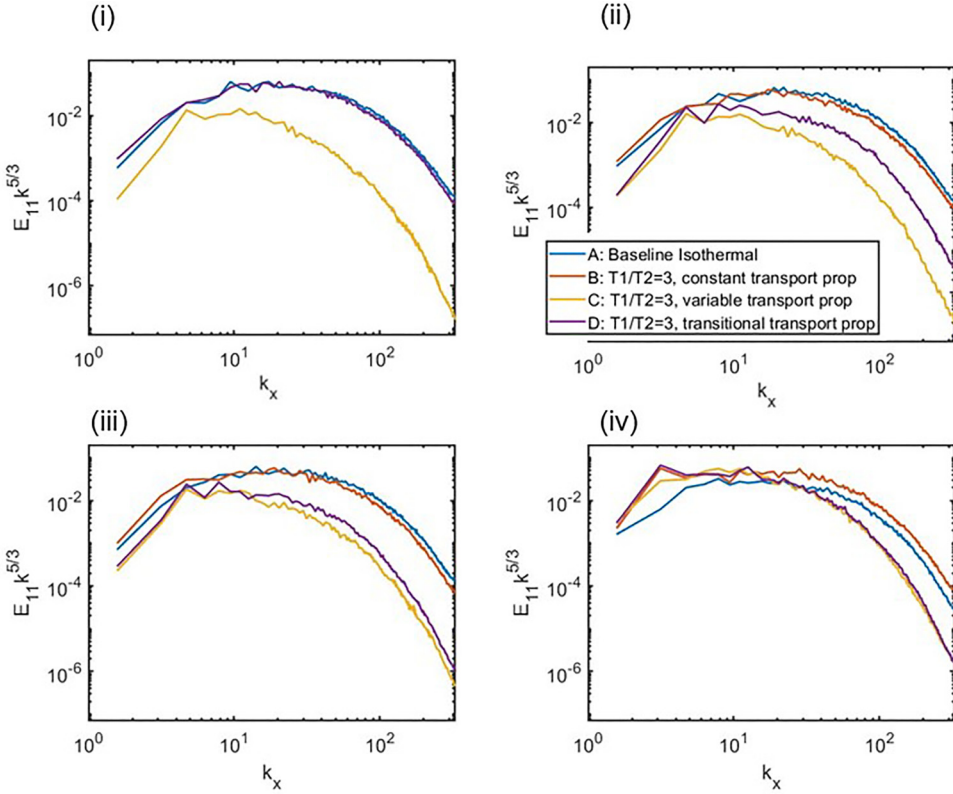
FIG. 23. Average 1D compensated u velocity spectras at the peak turbulence location at the various times described in Fig. 22(a): (i) initial state, (ii) peak of dissipation, (iii) middle of recovery period, and (iv) late-time state.

eigenvector. Heat transfer and the transport properties do not impact vorticity-strain alignment, as any differences in the distribution are indistinguishable from noise. The heat transfer does not affect mass fraction gradient-strain alignment, but transport properties decrease the alignment of χ_1 and χ_3 and increase the alignment of χ_2. Farther from the most turbulent region, we observe more
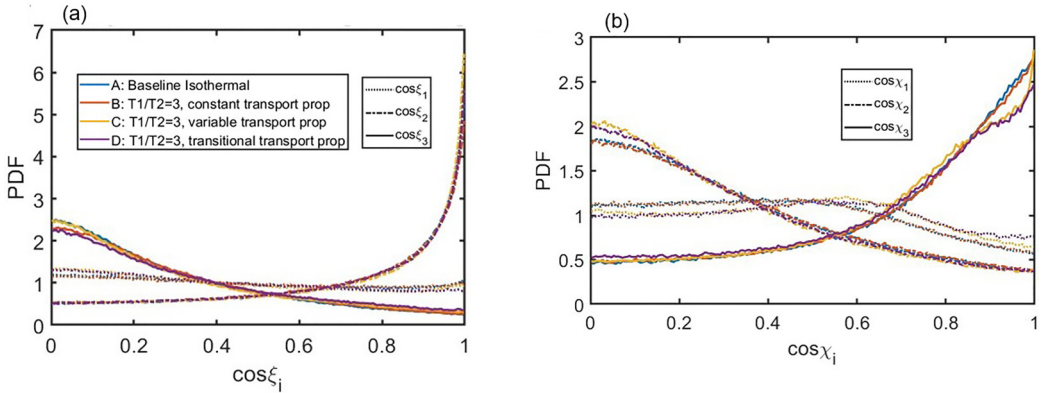

FIG. 24. PDFs of (a) vorticity-strain alignment angles and (b) mass fraction gradient-strain alignment angles at the peak turbulence location for the latest time in the simulation ($t = 13$).

extreme differences in mass fraction-strain alignments and the beginnings of some deviations in vorticity-strain alignment for cases C and D, but this should be expected because of the weaker turbulence activity. In general, vorticity alignment is not very sensitive to heat transfer or transport properties, and mass fraction gradient alignment is sensitive only to transport properties.

IV. DISCUSSION

With the moderate Atwood number and stratification, the baseline isothermal case A already deviates from the symmetries and expected scalings that have been documented for Boussinesq RT mixing. Therefore, this paper mainly focuses on comparing the differences between the variable temperature cases B, C, and D and the base case A. By using the three different transport property configurations, the sensitivity of various flow statistics to heat transfer itself or the accompanying transport property contrasts can be examined. In general, all scales of the flow, from the spike and bubble motions down to the dissipative regimes, are affected by heat conduction and transport properties. Heat conduction modifies the density field, a key factor in buoyancy driven flows, affecting the intensity and location of turbulent activity as the instability progresses. After sudden transport property changes, certain dynamical quantities such as vorticity and dissipation appear to lose memory of the past flow history and depend only on the current magnitude of the transport properties. The quantity and uniformity of the mixed fluid at various positions within the mixing zone, already asymmetrical to begin with in the baseline case, are further altered by all the temperature-related effects.

This analysis identifies temperature differences and all its associated effects as a key factor to consider in many ICF [51–53] and astrophysical simulations, and also expands on previous work on isothermal compressible RTI, which mainly focused on stratification effects. However, these simulations can serve as only a limited example of how thermal fluxes and transport properties can affect the flow dynamics and mixing of a compressible RT flow. It must be reiterated that any results described here in detail are highly specific to the particular molecular mass ratios and other parameters in the problem setup. Here the molecular mass of the bottom fluid is double that of the top fluid, so the top fluid is twice as isobarically compressible when changing temperature. Real applications may have significantly different background density profiles, involve species with more extreme or opposite molecular mass ratios explored in this study, and are not under hydrostatic equilibrium. Additionally, in ICF, there is extensive experimental evidence of strong self-generated electromagnetic fields generated during the implosion process [54–56], which can have a significant effect on the development of the flow instabilities [57,58]. To our knowledge, the exact nature of these electromagnetic fields is unclear, and we do not consider any electromagnetic effects in our study.

A. Numerical stiffness

The addition of strongly temperature-dependent transport properties introduces a large amount of numerical stiffness into the problem. The stability limit for time stepping becomes dependent on both the magnitude of the transport properties and their spatial derivatives. It has been found that the critical timestep required for stability at the onset in this compressible RTI problem can be even more strict than suggested by typical viscous explicit time-stepping restriction scalings such as $\Delta t \propto \rho \Delta x_i^2 / \mu$, as shown in Fig. 25. The critical time step Δt was determined by running a large set of simulations of a representative 1D version of the problem at different time-step sizes, and Δt is the minimum time-step size that prevents the solution from diverging. This stringent time-step requirement presents significant challenges when pushing towards higher temperature ratios, which is required to fully explore phenomena such as relaminarization and critical conditions for the survival or suppression of the RT instability. Additionally, the computational restriction places limits on domain size, but larger simulations are necessary for statistical convergence of higher-order moments of flow variables and detailed budget calculations.
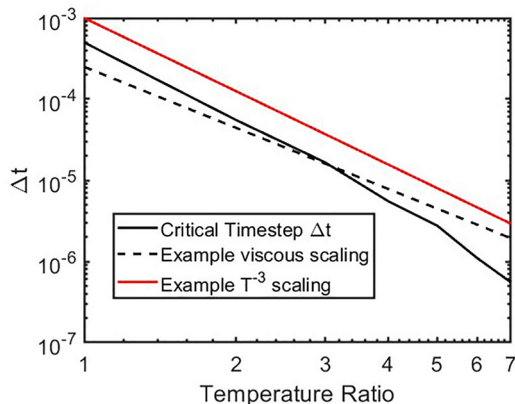
FIG. 25. Time-step stability limit for a representative 1D RT test case and comparison to various scalings.

V. CONCLUSIONS

Direct numerical simulations of the 3D fully compressible Rayleigh-Taylor instability are conducted for various temperature ratios and transport property variations. Inspired by ICF hot-spot conditions, the problem setup consists of colder, heavy fluid on top of hotter, light fluid. Comparisons among cases with constant transport properties (cases A, with isothermal background temperature, and B, with different temperatures for the heavy and light fluids), plasma-type temperature-dependent variable transport properties (case C), and transitional transport properties that vary in time (case D) allow the effects of heat transfer and transport property contrasts to be isolated. The temperature differences and their related effects further amplify the asymmetries already present in the baseline isothermal case, which has a moderate Atwood number and non-negligible stratification. However, some aspects of the flow display very little sensitivity to the heat conduction, transport properties, or both.

The main mechanism by which heat conduction affects the flow is through alteration of the density field, in turn influencing the strength of gravitational or buoyancy forces acting on the flow. The simulation cases B and C have different temperatures for the heavy and light fluids, which leads to non-negligible heat transfer across the interface. Due to the heat transfer, these cases lose the self-similar collapse of the average density profiles observed with the isothermal case A. As heat is deposited into the colder regions from the hotter regions, the fluids undergo local expansions and contractions, but the relative intensity of dilatation for the two fluids depends on both the temperature ratio and the relative molecular masses of the two species. Therefore, the spikes and bubbles, which begin at opposite temperatures and carry different molecular mass fluids, are affected very differently. In this problem setup, the heat transfer hinders penetration of the falling spikes, while extending the activity of the rising bubbles by affecting their densities.

A metric called the signed Atwood number At_l is introduced to describe the density field in more detail, allowing phenomena such as density reversals to be characterized. With heat transfer, the larger proportion of negative, lower magnitude At_l values on the light fluid side captures the density expansions undergone by the spikes, predicting the slowed down instability growth on the light fluid side and lessened turbulent activity. On the heavy fluid side, the prolonged and increased turbulent behavior can be explained by the wider range of At_l values sustained over time. Heat transfer shifts the peak of turbulent activity upwards into the heavy fluid and also increases the intensity of turbulence, as evidenced by the much higher maximum Re_t reached. In the most vortical or turbulent regions, the vorticity-strain alignment distributions are similar to other fully developed turbulent flows, and thus insensitive to heat transfer effects.

Transport properties that have a power-law scaling with temperature significantly increase the viscosity, thermal conductivity, and mass diffusivity on the hotter light fluid side. The higher viscosity, along with quicker density changes brought on by the boosted thermal conductivity further hinders spike penetration and delays bubble development. Interestingly, after temperature has become approximately equilibrated within the mixing layer, the constant and variable transport property cases show extremely similar density perturbation statistics on the heavy fluid side, as seen with the At_l and b profiles. The addition of variable transport properties further shifts turbulent activity upwards into the heavy fluid and also weakens it, reducing the intensity of velocity fluctuations and vorticity in the region of peak turbulence.

Mixing is also asymmetrically affected by heat transfer and transport properties. From the mixing midplane to the light fluid side, heat transfer slightly hinders mixing, increasing the amount of pure heavy fluid, but the fluid that is molecularly mixed becomes more uniform. In the same region, the variable transport properties cause a huge boost in the molecular diffusivity, decreasing the amount of pure heavy fluid and greatly increasing the uniformity of the mixed fluid. On the heavy fluid side, heat transfer causes a shift in the mixed fluid distribution from majority evenly mixed fluid towards a preference for majority heavy fluid, and adding variable transport properties has little impact. The mass fraction gradient-strain rate tensor alignment is sensitive only to the transport property magnitudes, but remains similar with the alignment found in other fully developed turbulent flows. The density-specific volume covariance was not found to be good indicator of the mixing state, due to heat transfer's influence on the density field.

Dissipation-viscosity independence does not apply in mixtures that have significant fluid dilatation or if one fluid has too high a viscosity. When transport properties suddenly change in magnitude, there is a peak in response for quantities such as dissipation and total mixing rate, TMR, then a transition period as the flow relaxes towards a final evolutionary state. Many of the dynamical quantities of the flow depend only on the current magnitudes of the transport properties. The vorticity distribution, velocity spectra, and average dissipation magnitudes for the variable property case C and the late time evolution in the transitional property case D exhibit many similarities. However, mixing responds differently, as the late-time evolution in the transitional case does not resemble any other configuration, suggesting a dependence on past mixing history in addition to the current transport property magnitudes.

The simulations have demonstrated how heat conduction and variable transport properties as a result of temperature differences can significantly affect the evolution of an RTI mixing layer. More simulations are needed to tackle temperature ratios high enough that local relaminarization and more significant effects on turbulence structure are observable in the variable transport property cases. It remains to be seen if the conclusions we have made at temperature ratio 3 and the corresponding transport property magnitude ratio of 15.6 for our variable/plasma-type property simulations continue to hold for higher temperature ratios. The results in this paper will be compared to those of analogous 2D simulations in future work, as current simulations targeting the relevant applications of interest are mostly still limited to two dimensions. In literature, many studies have uncovered significant differences between 2D and 3D RTI, so it would be useful to examine how dimensionality impacts the effects of heat transfer and transport properties.

[1] G. Boffetta and A. Mazzino, Incompressible Rayleigh–Taylor turbulence, Annu. Rev. Fluid Mech. **49**, 119 (2017).

[2] Y. Zhou, Rayleigh–Taylor and Richtmyer–Meshkov instability induced flow, turbulence, and mixing. I, Phys. Rep. **720–722**, 1 (2017).

[3] Y. Zhou, Rayleigh–Taylor and Richtmyer–Meshkov instability induced flow, turbulence, and mixing. II, Phys. Rep. **723–725**, 1 (2017).

[4] D. Livescu, Turbulence with large thermal and compositional density variations, Annu. Rev. Fluid Mech. **52**, 309 (2020).

[5] S. Gerashchenko and D. Livescu, Viscous effects on the Rayleigh-Taylor instability with background temperature gradient, Phys. Plasmas **23**, 072121 (2016).

[6] C. C. Kuranz, H.-S. Park, C. M. Huntington, A. R. Miles, B. A. Remington, T. Plewa, M. R. Trantham, H. F. Robey, D. Shvarts, A. Shimony *et al.*, How high energy fluxes may affect Rayleigh–Taylor instability growth in young supernova remnants, Nat. Commun. **9**, 1564 (2018).

[7] B. L. Creurer and S. Gauthier, A return toward equilibrium in a 2D Rayleigh–Taylor instability for compressible fluids with a multidomain adaptive Chebyshev method, Theor. Comput. Fluid Dyn. **22**, 125 (2008).

[8] S. Gauthier, Compressibility effects in Rayleigh–Taylor flows: Influence of the stratification, Phys. Scr. **T155**, 014012 (2013).

[9] S. Gauthier, Compressible Rayleigh–Taylor turbulent mixing layer between Newtonian miscible fluids, J. Fluid Mech. **830**, 211 (2017).

[10] S. J. Reckinger, D. Livescu, and O. V. Vasilyev, Adaptive wavelet collocation method simulations of Rayleigh–Taylor instability, Phys. Scr. **T142**, 014064 (2010).

[11] S. J. Reckinger, D. Livescu, and O. V. Vasilyev, Comprehensive numerical methodology for direct numerical simulations of compressible Rayleigh–Taylor instability, J. Comput. Phys. **313**, 181 (2016).

[12] S. A. Wieland, P. E. Hamlington, S. J. Reckinger, and D. Livescu, Effects of isothermal stratification strength on vorticity dynamics for single-mode compressible Rayleigh-Taylor instability, Phys. Rev. Fluids **4**, 093905 (2019).

[13] S. A. Wieland, Direct numerical simulations of the compressible low Atwood Rayleigh-Taylor instability, Ph.D. thesis, University of Colorado at Boulder (2019).

[14] R. Betti, K. Anderson, V. N. Goncharov, R. L. McCrory, D. D. Meyerhofer, S. Skupsky, and R. P. Town, Deceleration phase of inertial confinement fusion implosions, Phys. Plasmas **9**, 2277 (2002).

[15] S. A. Wieland, S. J. Reckinger, P. E. Hamlington, and D. Livescu, Effects of background stratification on the compressible Rayleigh-Taylor instability, in *47th AIAA Fluid Dynamics Conference, AIAA Aviation Forum and Exhibit* (AIAA Press, Denver, Colorado, 2017).

[16] F. Chen, A.-G. Xu, and G.-C. Zhang, Viscosity, heat conductivity, and Prandtl number effects in the Rayleigh–Taylor instability, Front. Phys. **11**, 114703 (2016).

[17] H. Zhang, R. Betti, R. Yan, D. Zhao, D. Shvarts, and H. Aluie, Self-similar multimode bubble-front evolution of the ablative Rayleigh-Taylor instability in two and three dimensions, Phys. Rev. Lett. **121**, 185002 (2018).

[18] J. Xin, R. Yan, Z.-H. Wan, D.-J. Sun, J. Zheng, H. Zhang, H. Aluie, and R. Betti, Two mode coupling of the ablative Rayleigh-Taylor instabilities, Phys. Plasmas **26**, 032703 (2019).

[19] D. Livescu, Compressibility effects on the Rayleigh–Taylor instability growth between immiscible fluids, Phys. Fluids **16**, 118 (2004).

[20] T. Luo and J. Wang, Effects of atwood number and stratification parameter on compressible multi-mode Rayleigh–Taylor instability, Phys. Fluids **33**, 115111 (2021).

[21] T. Luo and J. Wang, Mixing and energy transfer in compressible Rayleigh-Taylor turbulence for initial isothermal stratification, Phys. Rev. Fluids **7**, 104608 (2022).

[22] D. Aslangil and M. L. Wong, Study of iso-thermal stratification strength on 2D multi-mode compressible Rayleigh-Taylor instability, in *AIAA SciTech 2022 Forum* (AIAA Press, San Diego, CA, 2022).

[23] E. Vold, L. Yin, and B. J. Albright, Plasma transport simulations of Rayleigh–Taylor instability in near-ICF deceleration regimes, Phys. Plasmas **28**, 092709 (2021).

[24] R. K. Bera, Y. Song, and B. Srinivasan, The effect of viscosity and resistivity on Rayleigh–Taylor instability induced mixing in magnetized high-energy-density plasmas, J. Plasma Phys. **88**, 905880209 (2022).

[25] B. M. Haines, E. L. Vold, K. Molvig, C. Aldrich, and R. Rauenzahn, The effects of plasma diffusion and viscosity on turbulent instability growth, Phys. Plasmas **21**, 092306 (2014).

[26] G. Viciconte, B.-J. Grea, F. S. Godeferd, P. Arnault, and J. Clérouin, Sudden diffusion of turbulent mixing layers in weakly coupled plasmas under compression, Phys. Rev. E **100**, 063205 (2019).

[27] F. A. Jaberi, D. Livescu, and C. K. Madnia, Characteristics of chemically reacting compressible homogeneous turbulence, Phys. Fluids **12**, 1189 (2000).

[28] D. Livescu and D. Daniel, The influence of large variations in transport properties on homogeneous turbulence characteristics, in *16th Eur. Turbul. Conf.* (U.S. Department of Energy, Stockholm, Sweden, 2017).

[29] G. I. Taylor, Statistical theory of turbulence, Proc. R. Soc. Lond. **151**, 421 (1935).

[30] K. Lee, S. S. Girimaji, and J. Kerimo, Validity of Taylor's dissipation-viscosity independence postulate in variable-viscosity turbulent fluid mixtures, Phys. Rev. Lett. **101**, 074501 (2008).

[31] G. Kumar, S. S. Girimaji, and J. Kerimo, Preconditions and limitations of the postulate of scalar-dissipation–conductivity independence in a variable conductivity medium, Phys. Rev. E **84**, 046318 (2011).

[32] A. Subramaniam, Simulations of shock induced interfacial instabilities including materials with strength, Ph.D. thesis, Stanford University (2018).

[33] G. A. Blaisdell, N. N. Mansour, and W. C. Reynolds, Compressibility effects on the growth and structure of homogeneous turbulent shear flow, J. Fluid Mech. **256**, 443 (1993).

[34] E. L. Vold, A. S. Joglekar, M. I. Ortega, R. Moll, D. Fenn, and K. Molvig, Plasma viscosity with mass transport in spherical inertial confinement fusion implosion simulations, Phys. Plasmas **22**, 112708 (2015).

[35] S. Ganguli and S. K. Lele, Low Mach, compressibility, and finite size effects of localized uniform heat sources in a gas, Theor. Comput. Fluid Dyn. **33**, 341 (2019).

[36] V. Rana, H. Lim, J. Melvin, J. Glimm, B. Cheng, and D. H. Sharp, Mixing with applications to inertial-confinement-fusion implosions, Phys. Rev. E **95**, 013203 (2017).

[37] A. W. Cook and P. E. Dimotakis, Transition stages of Rayleigh–Taylor instability between miscible fluids, J. Fluid Mech. **443**, 69 (2001).

[38] D. Livescu, J. R. Ristorcelli, R. A. Gore, S. H. Dean, W. H. Cabot, and A. W. Cook, High-reynolds number Rayleigh–Taylor turbulence, J. Turbul. **10**, N13 (2009).

[39] J. P. Mellado, S. Sarkar, and Y. Zhou, Large-eddy simulation of Rayleigh-Taylor turbulence with compressible miscible fluids, Phys. Fluids **17**, 076101 (2005).

[40] D. Livescu, T. Wei, and P. Brady, Rayleigh-Taylor instability with gravity reversal, Physica D **417**, 132832 (2021).

[41] D. A. Donzis, P. K. Yeung, and K. R. Sreenivasan, Dissipation and enstrophy in isotropic turbulence: Resolution effects and scaling in direct numerical simulations, Phys. Fluids **20**, 045108 (2008).

[42] D. Buaria, A. Pumir, E. Bodenschatz, and P. K. Yeung, Extreme velocity gradients in turbulent flows, New J. Phys. **21**, 043004 (2019).

[43] J. R. Ristorcelli and T. T. Clark, Rayleigh–Taylor turbulence: Self-similar analysis and direct numerical simulations, J. Fluid Mech. **507**, 213 (2004).

[44] D. Livescu, J. R. Ristorcelli, M. R. Petersen, and R. A. Gore, New phenomena in variable-density Rayleigh–Taylor turbulence, Phys. Scr. **T142**, 014015 (2010).

[45] G. Dimonte, D. L. Youngs, A. Dimits, S. Weber, M. Marinak, S. Wunsch, C. Garasi, A. Robinson, M. J. Andrews, P. Ramaprabhu *et al.*, A comparative study of the turbulent Rayleigh–Taylor instability using high-resolution three-dimensional numerical simulations: The alpha-group collaboration, Phys. Fluids **16**, 1668 (2004).

[46] W. H. Cabot and A. W. Cook, Reynolds number effects on Rayleigh–Taylor instability with possible implications for type-Ia supernovae, Nat. Phys. **2**, 562 (2006).

[47] D. L. Youngs, Application of monotone integrated large eddy simulation to Rayleigh–Taylor mixing, Philos. Trans. R. Soc. A **367**, 2971 (2009).

[48] B. J. Olson and A. W. Cook, Rayleigh–Taylor shock waves, Phys. Fluids **19**, 128108 (2007).

[49] E. George and J. Glimm, Self-similarity of Rayleigh–Taylor mixing rates, Phys. Fluids **17**, 054101 (2005).

[50] D. Livescu and J. R. Ristorcelli, Variable-density mixing in buoyancy-driven turbulence, J. Fluid Mech. **605**, 145 (2008).

[51] H. Abu-Shawareb, R. Acree, P. Adams, J. Adams, B. Addis, R. Aden, P. Adrian, B. B. Afeyan, M. Aggleton, L. Aghaian *et al.* (Indirect Drive ICF Collaboration), Lawson criterion for ignition exceeded in an inertial fusion experiment, Phys. Rev. Lett. **129**, 075001 (2022).

[52] A. B. Zylstra, A. L. Kritcher, O. A. Hurricane, D. A. Callahan, J. E. Ralph, D. T. Casey, A. Pak, O. L. Landen, B. Bachmann, K. L. Baker *et al.*, Experimental achievement and signatures of ignition at the national ignition facility, Phys. Rev. E **106**, 025202 (2022).

[53] A. L. Kritcher, A. B. Zylstra, D. A. Callahan, O. A. Hurricane, C. R. Weber, D. S. Clark, C. V. Young, J. E. Ralph, D. T. Casey, A. Pak *et al.*, Design of an inertial fusion experiment exceeding the Lawson criterion for ignition, Phys. Rev. E **106**, 025201 (2022).

[54] C. K. Li, F. H. Séguin, J. A. Frenje, J. R. Rygg, R. D. Petrasso, R. P. Town, P. A. Amendt, S. P. Hatchett, O. L. Landen, A. J. Mackinnon *et al.*, Monoenergetic proton backlighter for measuring E and B fields and for radiographing implosions and high-energy density plasmas, Rev. Sci. Instrum. **77**, 10E725 (2006).

[55] C. K. Li, F. H. Séguin, J. R. Rygg, J. A. Frenje, M. Manuel, R. D. Petrasso, R. Betti, J. Delettrez, J. P. Knauer, F. Marshall *et al.*, Monoenergetic-proton-radiography measurements of implosion dynamics in direct-drive inertial-confinement fusion, Phys. Rev. Lett. **100**, 01 225001 (2008).

[56] C. K. Li, A. B. Zylstra, J. A. Frenje, F. H. Séguin, N. Sinenian, R. D. Petrasso, P. A. Amendt, R. Bionta, S. Friedrich, G. W. Collins *et al.*, Observation of strong electromagnetic fields around laser-entrance holes of ignition-scale hohlraums in inertial-confinement fusion experiments at the National Ignition Facility, New J. Phys. **15**, 025040 (2013).

[57] K. C. Tapinou, V. Wheatley, D. Bond, and I. Jahn, The Richtmyer–Meshkov instability of thermal, isotope and species interfaces in a five-moment multi-fluid plasma, J. Fluid Mech. **951**, A11 (2022).

[58] A. Briard, B.-J. Gréa, and F. Nguyen, Turbulent mixing in the vertical magnetic Rayleigh–Taylor instability, J. Fluid Mech. **979**, A8 (2024).